

The surface brightness of the Galaxy at the Solar Neighbourhood

A.-L. Melchior¹, F. Combes², and A. Gould^{3, *}

¹ LERMA, Université Pierre et Marie Curie and Observatoire de Paris, 61, avenue de l'Observatoire, F-75 014 Paris, France
e-mail: Anne-Laure.Melchior@obspm.fr

² LERMA, Observatoire de Paris, 61, avenue de l'Observatoire, F-75 014 Paris, France
e-mail: Francoise.Combes@obspm.fr

³ Department of Astronomy, Ohio State University, Columbus Ohio 43210, USA
e-mail: gould@astronomy.ohio-state.edu

Abstract. We present a new determination of the surface brightness of our Galaxy at the Solar Neighbourhood as observed from outside the Galaxy. We rely on various existing optical and infra-red surveys to obtain a multiwavelength estimate. On the one hand, scattered light does not contribute significantly to the surface brightness. On the other hand, optical and infrared integrated all-sky surveys (Pioneer 10/11 and COBE/DIRBE) show a systematically larger value than our synthetic local estimate based on Hipparcos data. This local estimate is also compatible with our Galactic simulations normalised at the Solar Neighbourhood and assuming an homogeneous stellar distribution. We interpret this disagreement as a signature of the presence of a local minimum of the stellar density compatible with Gould's belt. According to this result, the global luminosity of the Milky Way should follow the Tully-Fisher relation established for external galaxies.

Key words. (Galaxy:) solar neighbourhood—(Cosmology:) diffuse radiation—Radiation mechanisms: general—Methods: data analysis—ISM: general

1. Introduction

Modelling of the multiwavelength continuum emission of high- z galaxies is essential to simulate realistically the formation and evolution of galaxies as will be observed with the next generation of instruments. The data samples of galaxies are currently limited especially in the infrared and millimeter wavelengths, but will be significantly enlarged in the coming years. On the one hand, theoretical modelling based on physical principles actually relies on a large number of variables and requires well-sampled galaxy spectra to be constrained. On the other hand, empirical approaches (e.g. Guiderdoni et al. 1998; Dale et al. 2001) minimise the number of parameters to reproduce the current observations. Both approaches need to be validated with well-sampled continuum spectra of galaxies. It is customary to use the “Solar Neighbourhood” as a zero-point for these models. Even though various multiwavelength observations are available for the Galaxy and the Solar Neighbourhood, most authors quote Mathis et al. (1981), who were investigating the Local Interstellar Radiation Field. Although this work is robust to understand the absorption of photons by dust grains in the Local Neighbourhood, it did not intend to provide a spectral measurement of the surface brightness of our Galaxy at the Solar Neighbourhood as observed from outside the Galaxy.

Send offprint requests to:

* Visiting Astronomer, LPCC, Collège de France, 11, place Marcelin Berthelot, F-75231 Paris, France

In this paper, we compile various data sets to measure this quantity, which could be used as a zero-point for spectral modelling of external galaxies. We perform a cosecant averaging based on a plane parallel approximation for this measurement. In Sect. 2, we explain the basis for this approximation and its expected behaviour. We compare this approximation (integration in a cone) with the method usually used for external galaxies (integration in a cylinder) through simulations. In Sect. 3, we present a synthetic approach based on the Hipparcos data set and a stellar spectral flux library to estimate an optical spectrum of surface brightness of our Galaxy. We also present the two different types of integration (cone/cylinder), described here as corrected direct and indirect methods. In Sect. 4 and 5, we present a compilation of various all-sky surveys with the cosecant averaging method. In the optical, we use the stellar catalogues Tycho-2 and USNO-A2 as well as the Pioneer 10/11 integrated maps. In the infra-red, we project in cosech the COBE/DIRBE survey. Last, we discuss all these estimates.

2. Methods and simulations

The purpose of this paper is to determine at different wavelengths the surface brightness of our Galaxy at the Solar Neighbourhood as observed from outside the Galaxy. (Cf. Appendix B for a formal definition.) However, such an observational measurement imposes strong constraints: (1) we want to compare different wavelengths (which could be sam-

pled differently); (2) we would prefer to avoid the Galactic disc area, which is affected by crowding (stellar catalogues); (3) we would like to sample a significant volume in order to reduce local fluctuations.

The available all-sky surveys consist in stellar catalogues or integrated maps, at different wavelengths. In order to minimise the systematics due to this diversity, we adopt the same averaging procedure for each data set. The idea is to apply a cosecant averaging on the data to estimate the surface brightness of the Galaxy. This method, also called integration in a “cone”, satisfies the previous constraints, while approximating the integration in a cylinder, usually used to compute surface brightness of external galaxies. In this section, we present the different aspects of this approximation with respect to the standard method. Firstly, we present the modelling performed for our Galaxy and the methods used to compute the surface brightness. We describe the “integration in a cylinder”, which corresponds to the standard method to compute a surface brightness. We explain the difficulties due to our position near the plane of the Galaxy, and the corrections required to estimate the surface brightness corresponding to a face-on observation. In parallel, we present the alternate method used throughout this paper, called here “integration in a cone”. We discuss and compare the trends of both. Secondly, we simulate the cosec b projection that will be applied to stellar catalogues.

2.1. Definitions

We consider two extreme geometries for our Galaxy: (1) an exponential disc with scale length $h_R = 2.5$ kpc (Robin et al. 1992) and (variable) scale height¹ $h_Z(M_V)$, with a density normalised at the Solar neighbourhood; (2) a plane parallel model with a constant number density and a total thickness of $2h_Z = 240$ pc. In both cases, we assume that the Sun is located at a cylindrical Galactocentric radius $r_q = R_\odot = 8$ kpc, at $z_\odot = 15$ pc above the Galactic plane (Humphreys & Larsen 1995) and that the total extension of the Galaxy with respect to the centre is $R_{gal} = 14$ kpc. The numbers $n(r, b, l, M_V)$ of M_V stars per pc³ at the position (r, b, l) for the 2 geometries are as follows:

$$n^{D.Expon.}(r, b, l, M_V) = n_\odot(M_V) \exp(z_\odot/h_Z(M_V)) \exp(R_\odot/h_R) \exp(-r_q/h_R) \exp(-|z + z_\odot|/h_Z(M_V)) \quad (1)$$

with the cylindrical Galactocentric radius $r_q = (r_\odot^2 + r^2 \cos^2 b^2 - 2r_\odot r \cos b \cos l)^{1/2}$; the number density of M_V stars per pc³ $n_\odot(M_V) = \phi(M_V)$ is the luminosity function $\phi(M_V)$ at the Solar Neighbourhood, as defined in Appendix D; $z = r \sin b$ is the vertical position with respect to the Sun;

$$n^{PP}(r, b, l, M_V) = \begin{cases} n_\odot(M_V) \exp(z_\odot/h_Z(M_V)) & \text{if } |z + z_\odot| < h_Z, \\ 0 & \text{if } |z + z_\odot| \geq h_Z, \end{cases} \quad (2)$$

¹ Similarly to Miller & Scalo (1979), we take $h_Z = 80$ pc for $M_V \leq 0$, $h_Z = 250$ pc for $M_V \geq 8$, and a linear interpolation in between. We also consider a fixed scale height ($h_Z = 120$ pc), compatible with the variable scale height modelling in Fig. 4. See also Appendix D.

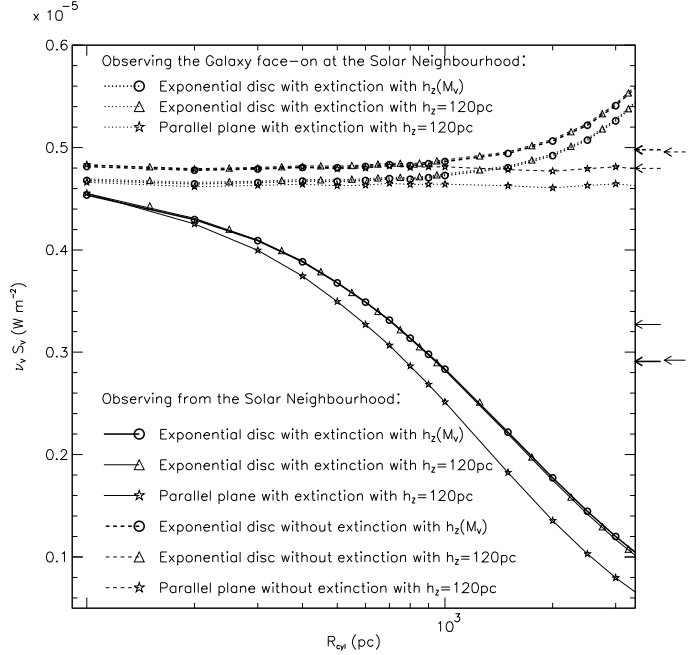


Fig. 1. Simulations. Surface Brightness in V band of the Milky Way as a function of the cylinder radius R_{cyl} for the models of Sect. 2. The cylinders corresponding to R_{cyl} are centered on the Sun and perpendicular to the Galactic plane. The curves with symbols correspond to the surface brightness computed with a cylinder for the exponential disc or plane parallel geometry. We consider two different observers: one observing from the Solar Neighbourhood and one observing the Galaxy face-on. We compare an ideal galaxy without extinction with the real configuration with extinction. The arrows on the right-hand side correspond to the integration in a cone with the cosecant law approximation, fitted for $1/\sin|b| \leq 6$. The caption for the line sizes (and types) of these horizontal lines are defined in Fig. 4.

We account for extinction with a uniform dust layer following the prescription provided and discussed in Appendix E.

2.1.1. Integration in a cylinder

We define the average surface brightness νS_V of our Galaxy at the Solar neighbourhood in the V band.

$$\nu S_V = \left[\int_{r,b,l,M_V} n(r, b, l, M_V) f(A_V(r, b)) L(M_V) r^2 \cos b \, dr \, db \, dl \, dM_V \right]_{r_q < R_{cyl}} / \pi R_{cyl}^2 \quad (3)$$

where $L(M_V)$ is the luminosity² of a star of M_V magnitude, $f(A_V(r, b)) = 10^{-0.4A_V(r, b)}$ is the extinction factor and R_{cyl} is the radius of the cylinder used to compute the surface brightness (see Fig. 1). In the absence of extinction and for $R_{cyl} < 2$ kpc, the two geometries are equivalent and the surface brightness is nearly independent of the cylinder radius. With extinction, the surface brightness measured from the Solar Neighbourhood decreases with increasing cylinder radius. This is due to the extinction affecting the $|b| < 90$ deg lines of sight crossing the dust plane. Of course, this effect is not observed when one

² We derive these luminosities in V with the formula $L(M_V) = C_V 10^{-0.4M_V} \times 4\pi(D_{(=10pc)})^2$, where $C_V = 1.97 \times 10^{-8} \text{ W m}^{-2}$.

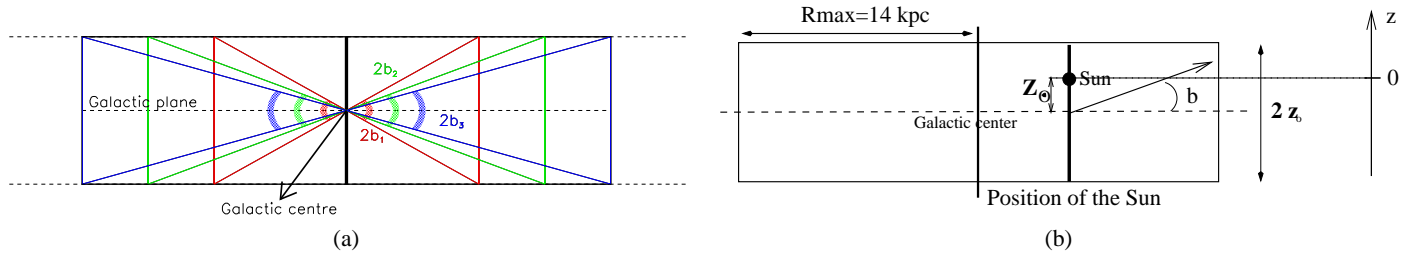


Fig. 3. Plane parallel approximation and cosecant method. The matter (HI gas or stars for instance) is assumed to be organised in planes parallel to the Galactic plane. **(a):** We assume an infinite thick sheet of uniform density centred on the Galactic plane. In this configuration, the column density perpendicular to the plane can be derived from the integration of the column density along various directions $b = b_1, b_2$ or $b_3\dots$ as defined in Eq. 5. **(b):** In this paper, we consider a truncated sheet for the plane parallel configuration, and then study this approximation for an exponential disc.

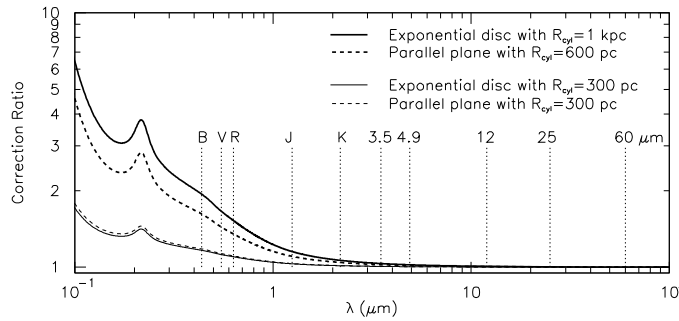


Fig. 2. Correction ratio as a function of wavelength necessary to derive the surface brightness of the Galaxy (observed face-on) from observations at the Solar Neighbourhood. We display the corrections (thick lines) for a cylinder of radius 1 kpc and 600 pc (corresponding to the $1/\sin b < 6$ cut for the cosecant law approximation). We also provide for comparison purposes the corresponding curves (thin lines) for a cylinder radius of 300 pc. For the wavelength dependence of the extinction, we assume $R_V = 3.1$ and use the prescription of Fitzpatrick (1999). The different wavelengths for which we project in cosech all-sky data are indicated (and numerical values provided in Table E.1).

computes the surface brightness for an observer of the face-on Galaxy, as only the lines of sight³ ($|b| = 90$ deg) perpendicular to the Galactic plane are integrated. In Fig. 2, we display the correction factor necessary to convert our local estimates (measured from the Solar Neighbourhood) into surface brightness of the face-on Galaxy (see also Tab. E.1).

2.1.2. Integration in a “cone” - cosecant-law approximation

We integrate the flux received at the Sun in a cone, according to the cosecant-law approximation (see Fig. 3). The slope of the corresponding function $\nu_\lambda I_\lambda(|b|)$ is the surface brightness of our Galaxy defined above, assuming an homogeneous stellar density galaxy.

$$\nu_V I_V(|b|) = 2 \times \int_{r,l,M_V} n(r, b, l, M_V) \frac{f(A_V(r, b)) L(M_V)}{4\pi} \cos b db dr dl dM_V \quad (4)$$

³ For our Galaxy, the extinction corresponding to the total disc thickness is 0.12 Vmag.

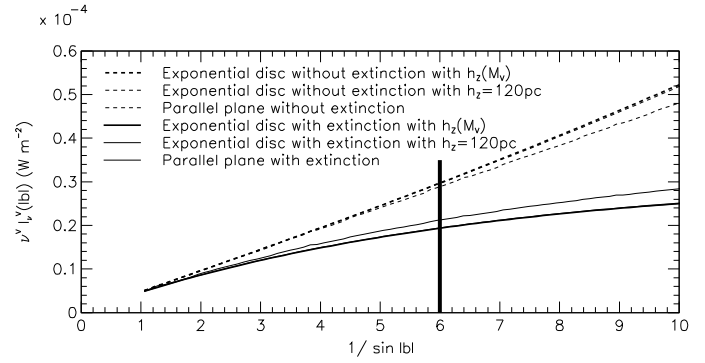


Fig. 4. Simulations. We present the cosecant laws computed for exponential disc and plane parallel geometries. We also consider the effect of extinction. When not indicated otherwise, the slopes are measured for $1/\sin |b| < 6$. The fixed and variable h_z geometries are barely distinguishable.

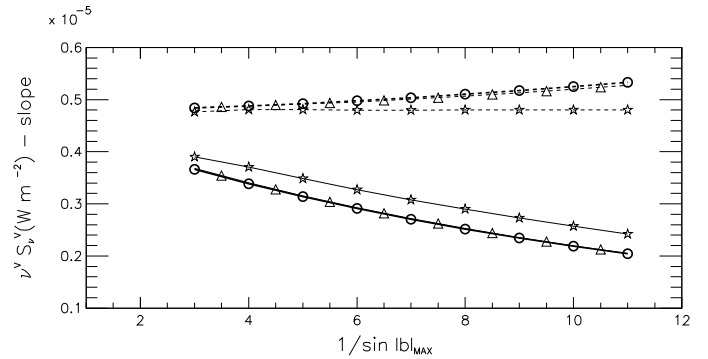


Fig. 5. Simulations. V Surface Brightness derived from the cosecant laws as a function of the chosen cut in $1/\sin |b|$. The symbols and lines follow the same convention as Fig. 1. The line widths and types are also defined in Fig. 4.

The normalisation factor in front of Eq. 4 is due to the normalisation of this method with respect to the integration in a cylinder. As explained in Appendix C, it has been determined for a uniform plane parallel geometry. Figure 4 displays the $\nu_V I_V(|b|)$ function, used to compute the surface brightness. To a good approximation, the curves are linear.

In the case of a plane parallel approximation without extinction, the slope of the $I_V(b)$ function with respect to $1/\sin b$

Table 1. Simulated V surface brightness expressed in different units. The first and second columns provide the surface brightness estimates derived from the Solar Neighbourhood (S.N.) and for the face-on Galaxy observed at the Solar Neighbourhood. The third column provides the estimate in the absence of extinction. The last column gives the unit of value provided in the different lines.

from S.N.	Face-on @ S.N.	without extinction	units
2.91×10^{-6}	4.72×10^{-6}	4.98×10^{-6}	W m^{-2}
9.7	15.6	16.5	$\text{L}_\odot \text{pc}^{-2}$
23.90	23.37	23.31	mag arcsec^{-2}

is equal to the value at $b = 90$ deg, namely:

$$\frac{I_V(b) - I_V(b = 90 \text{ deg})}{1/\sin b - 1} \sim I_V(b = 90 \text{ deg}) \quad (5)$$

For a linear function, Eq. 5 is an equality and is equivalent to $\nu_V S_V = I_V(b = 90 \text{ deg}) = I_V(b) \sin b$, where $\nu_V I_V(b = 90 \text{ deg})$ corresponds to the surface brightness. Figure 4 shows that, without extinction, the exponential disc geometry is very close to this approximation. In the presence of extinction, the two geometries (plane parallel and exponential disc) are also very close. Figure 5 displays the sensitivity of the cosecant-law approximation to the cut in $(1/\sin |b|)_{MAX}$.

2.1.3. Comparison

Plane parallel and exponential disc geometries provide very close results. In Figure 1, we compare the two modes of integration in V.

In the absence of extinction, the two modes of integration (in a cone and in a cylinder) are equivalent for $R_{cyl} < 2 \text{ kpc}$. With extinction, a flattening is observed for both methods. For integration in a cone, it is sensitive to the cut in $1/\sin b$ used to compute the slope (see Fig. 5). For integration in a cylinder, the surface brightness decreases as the radius of the cylinder considered increases (see Fig. 1).

As displayed in Fig. 1, we estimate that $1/\sin |b| \leq 6$ is the best compromise to sample the surface brightness of the Solar Neighbourhood over the whole spectral range. The cosecant-law approximation (computed with $1/\sin |b| \leq 6$) is compatible with the surface brightness computed in a cylinder of radius 1 kpc. The plane parallel model provides a similar equivalence at 600 pc. For this simple geometry, this radius can be compared to the maximum radius probed by the integration in a cone: $h_Z / \tan b_{max}$. For the parameter values considered, stars up to a radius of 710 pc are probed. For the exponential disc, we expect a similar difference (but asymmetric).

Table 1 provides the values thus obtained for the V surface brightness of our Galaxy at the Solar Neighbourhood for the different cases. It is important to note that the difference between the surface brightness estimated without extinction and the face-on Galaxy surface brightness (with extinction) is so small that scattered light can be neglected (less than 6% of the surface brightness).

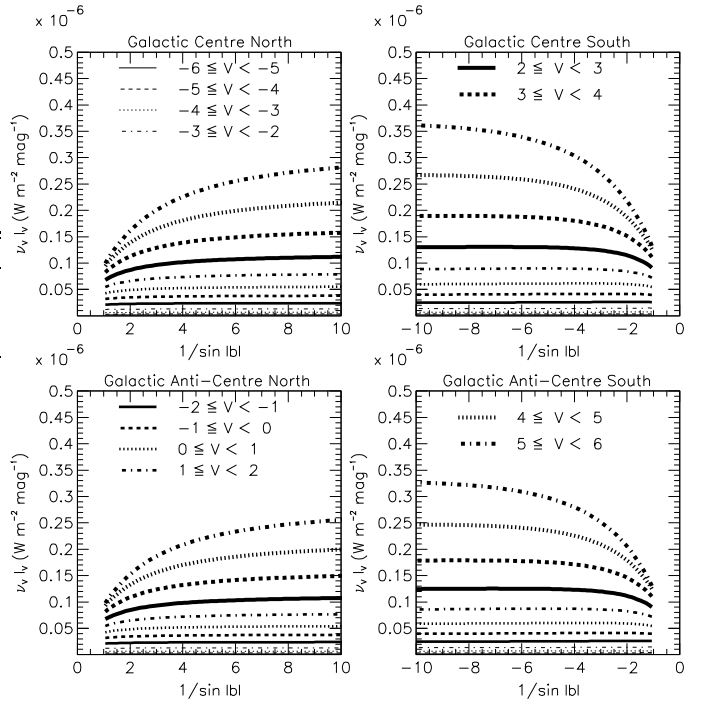


Fig. 6. Simulations in V with extinction. Integrated V flux in 1 mag bins as a function of $1/\sin |b|$ for the bright stars ($V < 6$).

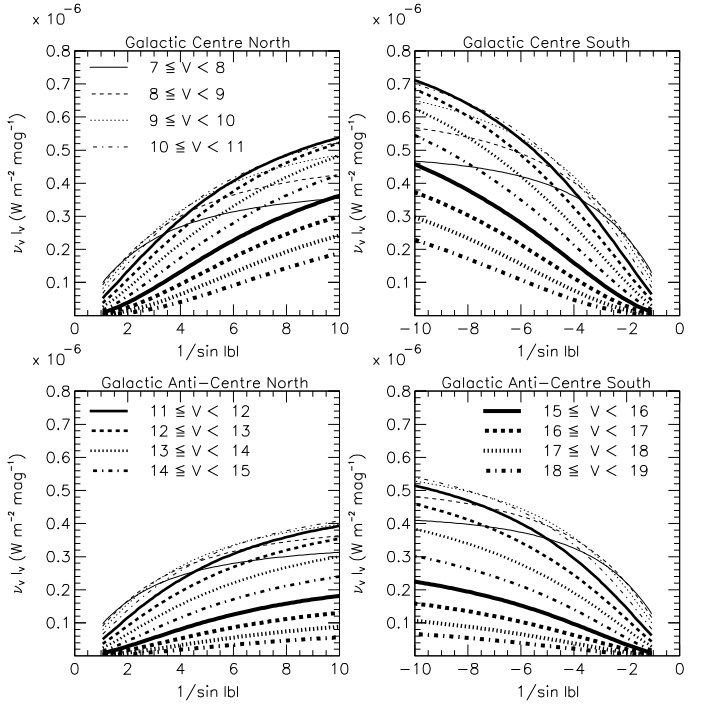


Fig. 7. Simulations in V with extinction. Integrated V flux in 1 mag bins as a function of $1/\sin |b|$ for fainter stars ($V \geq 7$).

2.2. Simulation of a catalogue reduction (observational procedure)

In the following, we will compile several whole sky stellar catalogues to measure the surface brightness of the Solar Neighbourhood. In order to understand the possible trends that could affect this observational procedure, we simulate this re-

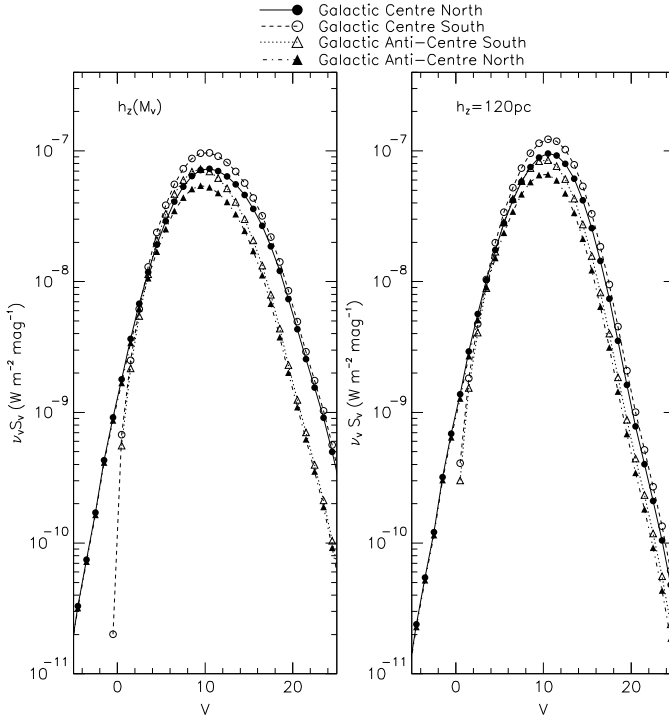


Fig. 8. Simulations in V with extinction. Contribution of each apparent V magnitude bin to the surface brightness for 4 sky areas. On the left (resp. right) panel, the stellar density (Eq. 1) is computed with a variable (resp. fixed) scale height $h_Z(M_V)$ (resp. $h_Z = 120$ pc).

duction for a V catalogue based on the cosecant-law approximation. We take our exponential geometry model with extinction and a variable scale height $h_Z(M_V)$ and decompose the $I(|b|)$ function into apparent V magnitude bins. We also divide the sky into 4 areas, in order to study asymmetries between the North and South Galactic hemispheres and the Galactic Centre and Anti-Centre directions. The sum of the slope of each bin provides the surface brightness at the Solar Neighbourhood.

Figures 6 and 7 display this simulation for $V < 6$ and $V \geq 7$ stars. The flux is higher in the direction of Galactic Centre. We observe a significant flattening for large $1/\sin|b|$, due to extinction. We also clearly detect the asymmetric position of the Sun above the Galactic plane ($z_\odot = 15$ pc). The left (resp. right) panel of Fig. 8 summarises the contribution of each apparent V magnitude bin to the surface brightness for $h_Z(M_V)$ (resp. $h_Z = 120$ pc). Table A.1 summarises the corresponding contribution per apparent magnitude bins. It also provides the fitted value at $b = 90^\circ$.

Each bin with $V < 2$ and $V > 21$ stars contributes to no more than about 1% of the surface brightness, while the main contributors (86.5% of the total surface brightness) are $5 < V < 16$ stars. Uncertainties on the very bright stars, which are often missed in stellar catalogue (due to their saturation, extinction in the stellar disc, etc.), and dim stars (close to the detection limit) will not bias the surface brightness estimate.

Note that this method, uncorrected for extinction, provides an estimate of the surface brightness computed from the Solar Neighbourhood, and has to be corrected as indicated in Fig. 2 and Table E.1 to obtain a face-on value.

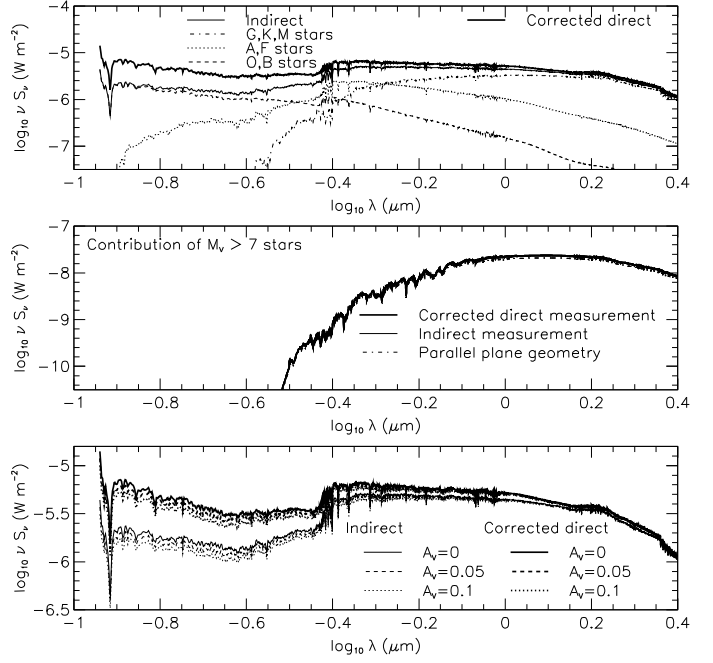


Fig. 9. Corrected direct and indirect synthetic estimates of the surface brightness of our Galaxy at the Solar Neighbourhood. In the top panel, we display the two estimates obtained with the compilation of the $V < 7.3$ Hipparcos Catalogue stars. For the indirect estimate, we indicate the contribution of the different types of stars. In the middle panel, we display the contribution of $M_V > 7$ stars with our simulation tool for different configurations. We also consider $\pm 1\sigma$ luminosity functions to estimate the scatter due to uncertainties in the luminosity function. These dim stars mainly contribute to the near-infrared part of the spectrum, but this integrated surface brightness remains an order of magnitude below their bright counter-parts. In the bottom panel, we study the influence of the extinction, perpendicular to the Galactic plane, which might have a marginal influence in the UV. We assume a fixed extinction A_V applies to the whole population.

3. Stellar Surface Brightness: a synthetic approach with the Hipparcos data

The Hipparcos Catalogue (Perryman et al. 1997; van Leeuwen et al. 1997) with the Hipparcos Input Catalogue (HIC) (Turon et al. 1992, 1995) constitute a unique database to explore the Solar Neighbourhood. Spectral type, parallax, and V magnitude are provided for each $V < 7.3$ star. We restrict the sample to 13 374 stars with a 3σ parallax and with the constraints on the completion limits described in Appendix D. In the following, we use the stellar spectral flux library from Pickles (1998) to produce synthetic spectra: a spectrum is associated with each star and normalised to the observed V flux. Hipparcos stars are then combined in two different ways to get estimates of the surface brightness. In Sect. 3.1, we directly sum the flux of the observed stars with a $\sin|b|$ weighting. However, this direct measurement requires a volume correction due to the apparent magnitude limit of the sample used. This corrected direct measurement corresponds to the cosecant averaging (integration in a cone). In Sect. 3.2, we compute the surface brightness with the luminosity of the stars with the integration in the cylinder approach. Appropriate volume corrections are also required.

3.1. Corrected direct measurement of starlight: a synthetic spectrum

The cosecant-law approximation (see Eq. 5) enables to compute directly the surface brightness as the sum of the stellar fluxes weighted by $\sin |b|$. Even though the amount of dust is small at the Solar neighbourhood, it significantly affects the surface brightness computation (see Fig. 1). We have shown in Sect. 2 that the surface brightness of our Galaxy observed face-on is very close to the surface brightness computed for a Galaxy without dust. Hence, we subtract the extinction to each star relying on our dust modelling (see Appendix E), and obtain the lower bound:

$$\begin{aligned} vS_v &> 2 \times \sum_i^{\text{all stars}} vF_v(M_V, S pT) / f(A_V) \times \sin |b| \\ &> 2 \times \sum_i^{\text{all stars}} \frac{L_\lambda(M_V, S pT)}{4\pi r_i^2} \times \sin |b| \end{aligned} \quad (6)$$

where $F_v(M_V, S pT)$ (resp. $L_\lambda(M_V, S pT)$) is the flux (resp. luminosity) spectrum in $\text{W m}^{-2} \text{Hz}^{-1}$ (resp. W) corresponding to a star with a magnitude M_V and a spectral type SpT, and r_i the actual distance of this star.

According to our simulations (Table A.1), the cut in apparent magnitude ($V < 7.3$) limits our sensitivity to 17% of the total V stellar surface brightness. We apply a volume correction relying on the knowledge of the Hipparcos parallaxes together with the well-defined completeness limit ($V < 7.3$): each absolute magnitude bin ($M_V - \frac{1}{2} \leq m < M_V + \frac{1}{2}$) is complete within a radius $R(M_V + \frac{1}{2})$ (see Appendix D.2). We compute

$$\begin{aligned} vS_v = 2 \times \sum_i^{M_V < 7} \sum_{[M_V - \frac{1}{2}, M_V + \frac{1}{2}]}^{\text{x}_i \in} & \frac{L_\lambda(x_i, S pT) \sin |b|}{4\pi r^2} \times f_i^{LF} \\ & \times \frac{W_*^{sph}(R_{max})}{W_*^{sph}(R(x_i))} \end{aligned} \quad (7)$$

here $L_\lambda(x_i, S pT)$ is the spectrum (in W) corresponding to a star with a magnitude $M_V - \frac{1}{2} \leq x_i < M_V + \frac{1}{2}$ and a spectral type SpT, f_i^{LF} is the correction of the luminosity function provided in Fig. D.4 applied for stars with $M_V \leq -1.5$, and $R_{max} = 1\text{kpc}$ is the cylinder radius discussed in Sect. 2. The last factor corresponds to the volume correction with: $W_*^{sph}(y) = \int_{r < y} n(r, b, l) \sin |b| / r^2 dv, dv = \cos(b) db dl dr$. $W_*^{sph}(y)$ corresponds to the stellar surface density weighted by $\sin |b| / r^2$ computed within a sphere of radius y . $W_*^{sph}(R(x_i))$ is computed for each magnitude bin, while $W_*^{sph}(R_{max})$ is obtained with a weighted sphere with the radius of the cylinder radius R_{max} . The corresponding spectrum is displayed in Figure 9. We check that if we take $W_*^{sph}(5R_{max})$ instead of $W_*^{sph}(R_{max})$, the estimate of the surface brightness increases by less than 14.5%.

This measurement takes into account the real distribution of stars but assumes an smooth and homogeneous distribution of stars of the LF along the exponential profile of the Milky Way for the corrections.

3.2. Indirect measurement of starlight: a synthetic spectrum

The second possibility is to compute the surface brightness as the mean stellar luminosity spectrum per unit area at the Solar Neighbourhood. We rely on Hipparcos data for intrinsically bright stars ($M_V < 7$) and perform the appropriate corrections, as follows:

$$vI_V = \sum_i^{M_V < 7} \sum_{[M_V - \frac{1}{2}, M_V + \frac{1}{2}]}^{\text{x}_i \in} \frac{L_\lambda(x_i, S pT)}{\pi R(x_i)^2} \times f_i^{LF} \times \frac{\Sigma_i^{cyl}}{\Sigma_i^{sph}} \quad (8)$$

where $L_\lambda(M_V, S pT)$ is the spectrum (in W) corresponding to a star with a magnitude M_V and a spectral type SpT, f_i^{LF} is the correction of the luminosity function. The last factor corresponds to the volume correction for each magnitude bin. Σ_i^{cyl} is the stellar surface density computed for the cylinder of radius R_{max} , while Σ_i^{sph} is the stellar surface density integrated over a sphere of radius $R(x_i)$ normalised to the surface $\pi R(x_i)^2$.

This measurement assumes a smooth homogeneous distribution of the stars and a uniform LF along the exponential profile of the Milky Way.

3.3. Discussion

Figure 9 presents the corrected direct and indirect estimates. The two curves are very close in the optical and near-infrared, while they differ significantly in the UV. This difference, which cannot be explained with the extinction (see bottom panel of Fig. 9), is understood as due to the inhomogeneous distribution of the OB associations (de Zeeuw et al. 1999, see also Appendix D.3). If we remove the very bright stars ($M_V < -4.5$), the corrected direct estimate is reduced in the UV. If we remove the bright stars ($M_V < -1.5$), all the discrepancies are removed.

The corrected direct estimate, based on the fluxes, is very sensitive to the anisotropic distribution of OB associations, while the indirect estimate is more robust, as it is based on luminosities, but does not account for the real spatial distribution of stars. The uncertainties on the bright end of the LF (see Fig. D.1) are also a source of error. By chance, our indirect estimate is in good agreement with the UV measurements of Gondhalekar et al. (1980) (see Fig. 16). However, it is a different quantity that has been measured: the sum of the UV light over the whole sky (S2/68 Sky-survey TD1-satellite data) without any extinction correction. This might mean that, due to an obvious selection bias, we detect only stars that are moderately extinguished, but this might also be a coincidence as the measured quantities are different.

The significant difference of our two estimates in the UV range is due to the irregular distribution of OB stars (considered homogeneous in the indirect estimate).

The surface brightness obtained in the optical can be compared with the study of Flynn et al. (2006). These authors use accurate data on the local luminosity function and the disc's vertical structure to measure the following surface brightnesses (see their Table 5): $\mu_B = 23.51 \text{ mag.arcsec}^{-2}$, $\mu_V = 22.93 \text{ mag.arcsec}^{-2}$, and $\mu_I = 22.03 \text{ mag.arcsec}^{-2}$. These values are

Table 2. Contribution of the $B < 6$ stars to the surface brightness (see Fig. 14). 2783 Hipparcos stars are thus been used. Values with the observed extinction are provided together with the values corrected for extinction.

λ (μm)	With extinction	Without extinction
0.440 (B_J)	5.640×10^{-7}	6.186×10^{-7}

in good agreement with our corrected direct estimates (see Tables 6 and 7). Our indirect estimates are slightly weaker for the reasons discussed above.

4. Optical surface brightness

4.1. USNO-A2 and TYCHO-2 data

The USNO-A2 B and R magnitudes have been calibrated as explained in Appendix G.

4.1.1. B measurements

Figures 10 and 11 display the cosecant laws obtained for 4 sky areas with the USNO-A2 and TYCHO-2 stellar catalogues and for each magnitude bin. Table A.2 summarises the slopes measured with the fit to the cosecant laws and provides a comparison with simulations. These simulations are based on the method described in Sect. 2.2. A B luminosity function has been derived from the V luminosity function displayed in Fig. D.1, assuming that 50% of the $V < 2$ stars are red giants. We relying on Lang (1992, p:137-145) to relate the V absolute

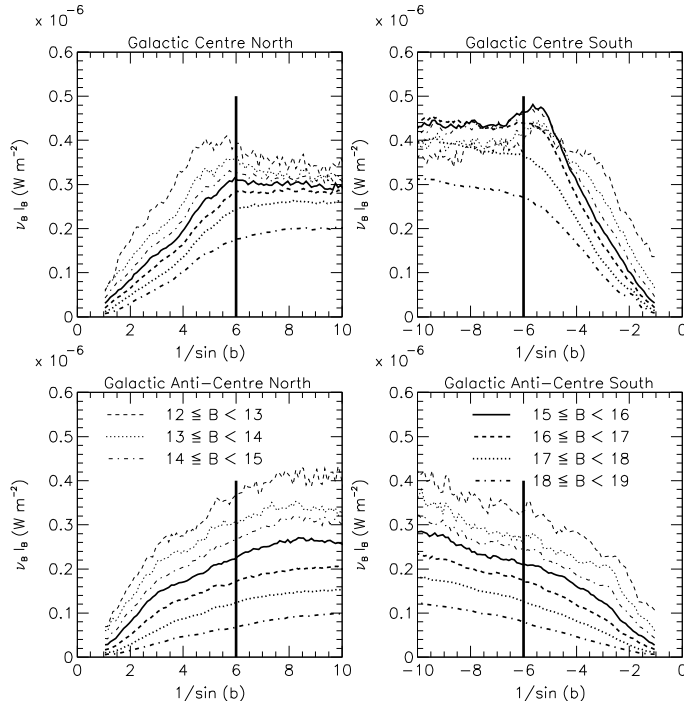


Fig. 10. Cosecant laws for $12 \leq B < 19$ stars from the USNO-A2 catalogue. Irregularities, significant towards the Galactic centre, are minimised by our cut $1/\sin|b| < 6$. (See Table A.2.)

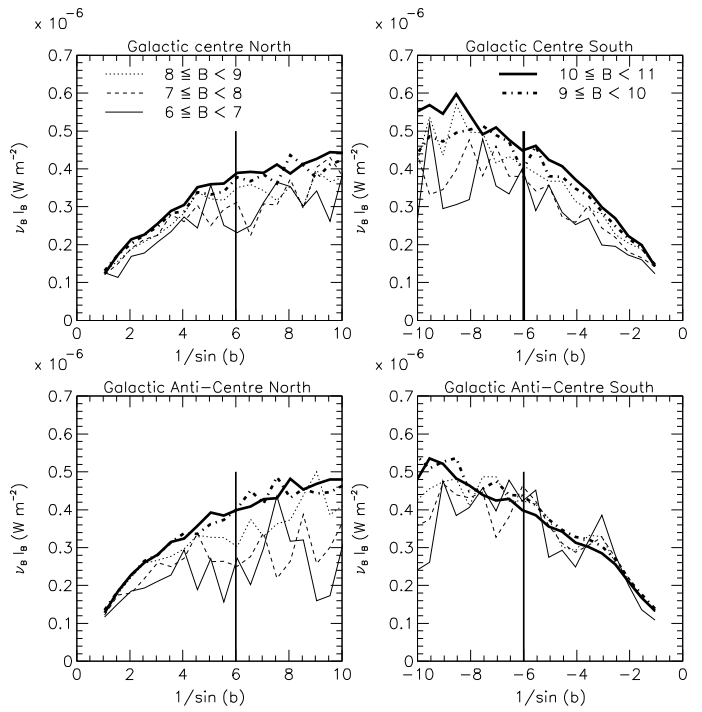


Fig. 11. Similar to Fig. 10 for B cosecant laws computed for $6 \leq B < 11$ TYCHO-2 stars. (See Table A.2.)

Table 3. Contribution of the $R < 6$ stars to the surface brightness computed the same way as those displayed in Fig. 14. 7010 Hipparcos stars are thus considered. Values with the observed extinction are provided together with the values corrected for extinction.

λ (μm)	With extinction	Without extinction
0.640 (R)	6.98×10^{-7}	7.41×10^{-7}

magnitudes to spectral types from Pickles (1998), and to perform this transformation. We thus find excellent agreement between our simulations and the TYCHO-2 data. The USNO-A2 data provide estimates systematically larger than our simulations. The emission in the Galactic Centre South direction is perturbed as displayed in Fig. 10. Note that simulations show that $B > 19$ stars do not contribute more than a few percent to the total surface brightness.

We combine the B USNO-A2 and TYCHO-2 estimates for $B > 6$ stars with the synthetic uncorrected estimate based on ($B < 6$) Hipparcos stars (see Table 2 and Fig. 14), and correct the extinction with the global factor provided in Fig. 2 and Table E.1, as follows:

$$v_B S_B = (5.640 \times 10^{-7} + 3.004 \times 10^{-6}) \times 1.72 = 6.13 \times 10^{-6} \text{ W m}^{-2} = 23.51 \text{ mag arcsec}^{-2} \quad (9)$$

$$(10)$$

4.1.2. R measurements

The data reduction of the R measurements of the calibrated USNO-A2 data is presented in Table A.3 and Figure 12. We clearly observe an excess of the stellar data with $12 < R < 18$

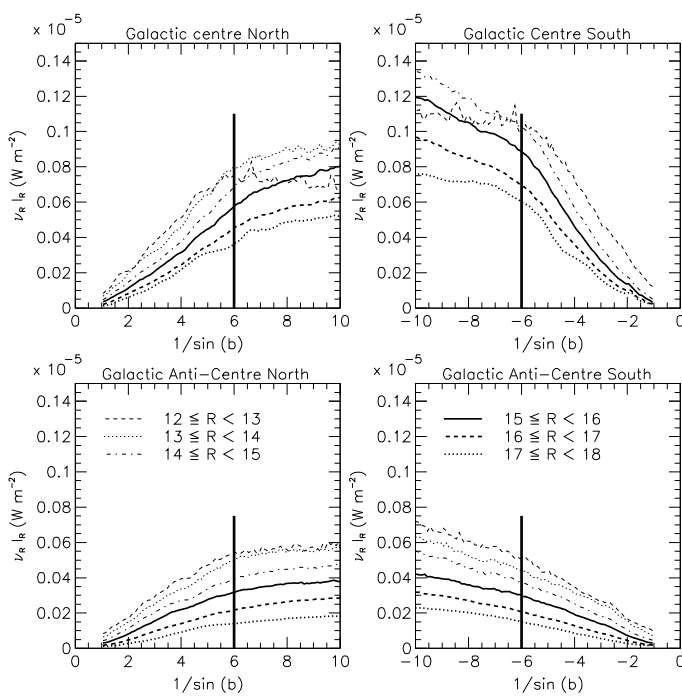


Fig. 12. Integrated R fluxes as a function of $1/\sin(b)$ computed with the USNO-A2 data for $12 \leq R < 18$ stars. We decompose the contributions originating from different sky areas. No correction has been applied. (See Table A.3.)

with respect to our simulation⁴. This cannot be accounted for the thick disc dominated by dim stars ($M_V > 4$), which do not contribute significant to the surface brightness (see Fig. D.2). We carefully check with the USNO-B1 (Monet et al. 2003) catalogue that our calibration is satisfactory. In addition, this excess has been confirmed with the CCD UCAC-1 data (see Appendix F).

We complete the $12 \leq R < 18$ USNO-A2 estimate with simulations presented in Table A.3, and correct the extinction with the global factor provided in Fig. 2 and Table E.1, as follows:

$$\nu_R S_R = (2.205 \times 10^{-6} + 2.555 \times 10^{-6}) \times 1.41 = 6.71 \times 10^{-6} \text{ W m}^{-2} = 22.6 \text{ mag arcsec}^{-2} \quad (11)$$

$$(12)$$

4.2. Pioneer 10/11 data

As discussed in Gordon et al. (1998) (see also Leinert et al. 1998), the Pioneer 10/11 data provide an excellent all-sky survey in B ($0.437\mu\text{m}$) and R ($0.644\mu\text{m}$) for the study of integrated flux. In contrast to the Tycho star mapper background analysis of Wicenec & van Leeuwen (1995), the Pioneer 10/11 data taken beyond 3.26 AU provide sky-maps devoid of detectable zodiacal light. We use here the Pioneer 10/11 maps kindly provided by K. Gordon (see Gordon et al. 1998 and Witt, Gordon

⁴ To account for red giants, we apply in R the modification of the luminosity function described in Sect. 4.1.1 to perform this simulation.

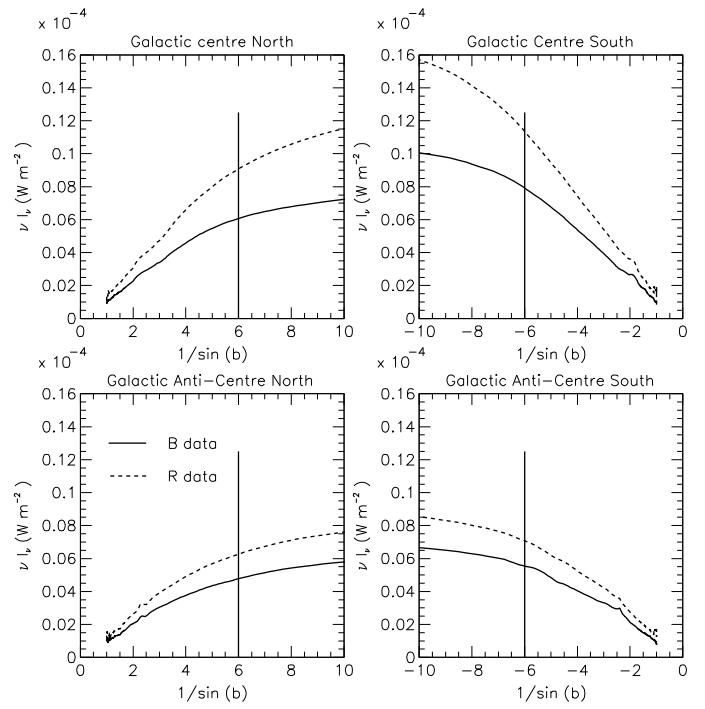


Fig. 13. Cosecant laws for Pioneer 10/11 B (full-line) and R (dashed-line) data (Gordon et al. 1998). This corresponds to $V > 6.5$ stars and diffuse emission. There is a hole in the Galactic Anti-Centre North area (bottom left) that has been removed. No correction has been applied. (See Table 4.)

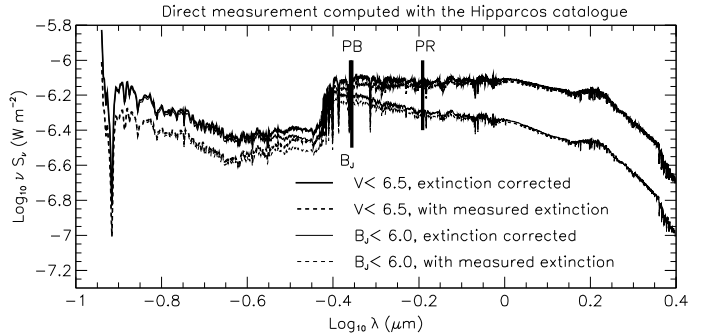


Fig. 14. Direct contribution of bright stars to the surface brightness. These synthetic estimates have been computed with Eq. 6 for $V < 6.5$ stars and for $B < 6$ stars from the Hipparcos catalogue. 8 013 and 2 783 stars have thus been used, while the few neglected stars do not contribute to more than 10% in V (see Table 5). The vertical lines indicate the wavelengths discussed in the text (B_J and Pioneer B/R). Note that the extinction considered here is the extinction affecting each individual star not the global extinction perpendicular to the Galactic plane.

& Cohen, in preparation): they correspond to the first iteration maps discussed in Gordon et al. (1998). These maps contain all relevant flux (starlight and possible diffuse components), except for stars brighter than $V = 6.5$ (see Toller et al. 1987). Figure 13 displays the $1/\sin(b)$ laws obtained in B and R for the different sky areas, while Table 4 provides the corresponding slopes. The R fluxes are systematically larger than the B fluxes: as discussed in the following, this is a consequence of the extinction.

Table 4. $B(0.437\mu\text{m})$ and $R(0.644\mu\text{m})$ (Pioneer 10/11 derived) surface brightness, given in 10^{-9} W m^{-2} . We give the values fitted for $1/\sin(b) < 6$ (see Fig. 13). The surface brightness thus obtained accounts for the $V > 6.5$ stars as well as for a possible diffuse component.

$\lambda (\mu\text{m})$	Galactic Centre				Galactic Anti-Centre							
	North		South		North		South					
	$ b = 90^\circ$	slope	$ b = 90^\circ$	slope	$ b = 90^\circ$	slope	$ b = 90^\circ$	slope				
0.437 (B)	1050.	1148.	1048.	1444.	1046.	886.	996.	1040.				
0.644 (R)	1368.	1684.	1542.	1958.	1320.	1164.	1500.	1234.				
	Sum											
0.437 (B)	2098. ($ b = 90^\circ$), 2592. (slope)				2042. ($ b = 90^\circ$), 1926. (slope)							
0.644 (R)	2910. ($ b = 90^\circ$), 3642. (slope)				2820. ($ b = 90^\circ$), 2398. (slope)							
	Total B (0.437μm) value: 4140. ($b = 90^\circ$), 4518. (slope)											
	Total R (0.644μm) value: 5730. ($b = 90^\circ$), 6040 (slope)											

Table 5. Contribution of the $V < 6.5$ stars to the surface brightness (see Fig. 14). Values with the observed extinction are provided together with the values corrected for extinction. We estimate that we do not miss¹ more than 3% of the brightness in V.

$\lambda (\mu\text{m})$	With extinction	Without extinction
0.437 (B)	7.020×10^{-7}	7.751×10^{-7}
0.644 (R)	7.261×10^{-7}	7.699×10^{-7}
V bad stars ¹	2.465×10^{-8}	

¹ This corresponds to stars with uncertain parallax or unspecified spectral type neglected for the previous direct estimates.

Relying on Eq. 5, we compute the contribution of the bright ($V < 6.5$) stars, independently with a synthetic direct estimate based on the Hipparcos Catalogue, which is complete for these stars. We nevertheless neglect stars with uncertain parallax or undefined spectral type, but estimate that they do not contribute more than 10% in V.

We combine the Pioneer B and R estimates with the ($V < 6.5$) stars synthetic uncorrected estimates, and correct the extinction with the global factor provided in Fig. 2 and Table E.1 (see also Appendix E), as follows:

$$S_B = (7.02 \times 10^{-7} + 4.52 \times 10^{-6}) \times 1.72 = 8.98 \times 10^{-6} \text{ W m}^{-2} = 23.1 \text{ mag arcsec}^{-2} \quad (13)$$

$$S_R = (7.26 \times 10^{-7} + 6.04 \times 10^{-6}) \times 1.41 = 9.54 \times 10^{-6} \text{ W m}^{-2} = 22.3 \text{ mag arcsec}^{-2} \quad (14)$$

Our estimate is brighter than the estimate of the surface brightness obtained in B by van der Kruit (1986) with the Pioneer data ($\mu_B = 23.8 \pm 0.1 \text{ mag arcsec}^{-2}$), who did not correct for extinction.

The values obtained here are systematic brighter than our synthetic estimates and than the local values provided by Flynn et al. (2006). As later discussed in Sect. 6, we suggest that this disagreement is due to a larger volume probed with the USNO-A2 and Pioneer 10/11 all-sky surveys.

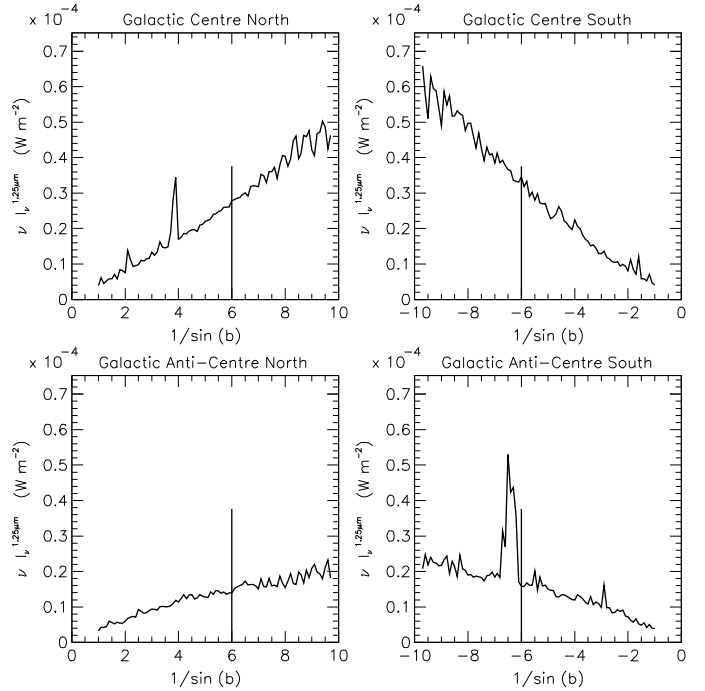


Fig. 15. Cosecant laws for the $1.25\mu\text{m}$ COBE/DIRBE data averaged over Galactic latitude. These values are derived from Zodi-Subtracted Mission Average (ZSMA) data distribution. The sharp peaks correspond to bright stars ($0 < V < 1$ and M type). We performed similar plots for the other 9 COBE/DIRBE available wavelengths. Wiggles observed for $1/\sin(b) > 6$ are due to the COBE/DIRBE sampling (pixels of $0.32^\circ \times 0.32^\circ$).

5. Infrared surface brightness: COBE/DIRBE data

We consider the Zodi-Subtracted Mission Average (ZSMA) maps (Kelsall et al. 1998) from the COBE/DIRBE project. We plot the cosecant laws for the wavelengths $1.25, 2.2, 3.5, 4.9, 12, 25, 60, 100, 140$ and $240\mu\text{m}$ as shown in Figure 15 (for $1.25\mu\text{m}$). We then perform a linear fit (slope and $|b| = 90^\circ$ values) with the parameters provided in Table A.4. We are sensitive to bright point sources (like Betelgeuse) up to $4.9\mu\text{m}$, that we eliminate with a 5σ clip when necessary. Unlike Boulanger & Pérault (1988), we do not subtract nearby dust complexes

from the study as we are interested in the light of all the components. Otherwise, we observe quite a linear behaviour except at 12 and 25 μm where the light emission is very irregular, as observed by Boulanger & Péault (1988) with IRAS data. These data exhibit a large value of the $|b| = 90^\circ$ intensity and a small value of the slope. This large $|b| = 90^\circ$ intensity is characteristic of a “non-Galactic” or at least irregular behaviour, and also seems to affect marginally the 4.90 μm data. At 12 and 25 μm , we observe an unexplained excess for $1/\sin|b| < 2$ ($b > 30^\circ$), which affects the fit. A strange behaviour was also noted by Boulanger & Péault (1988) in this area and interpreted as a consequence of imperfect Zodiacial light subtraction. Hence, we perform the fit for $2 < 1/\sin|b| < 6$ at these wavelengths in order to minimise the effect, but these measurements are probably still affected by noise and systematic effects. Note that Arendt et al. (1998), who studied the Galactic foreground from the same ZSMA data, have identified similar spurious effects and explained them with residuals of the Zodiacial light subtraction.

For $\lambda < 5\mu\text{m}$, we observe the expected asymmetry between the North and South hemispheres due to the position of the Sun above the Galactic plane: the integrated radiation intensity measured in the Galactic Center (resp. Anti-Centre) South panel is larger than the one measured in the Galactic Center (resp. Anti-Centre) North panel. At longer wavelengths, we observe an inverted behaviour: the radiation intensity measured in Galactic North panels is larger than the one measured in the South panels. This is explained by the presence of a warp of the Galactic disc (beyond 12 kpc) towards the North and Galactic Centre (see e.g. Burton & Te Lintel Hekkert 1986; Wouterloot, Brand, Burton, & Kwee 1990). Last, for $\lambda \geq 60\mu\text{m}$, we are affected by nearby complexes (that we choose not to remove): this tends to enlarge the uncertainties but accounts for local fluxes. This probably explains in part the relatively low values of the intercepts ($|b| = 90^\circ$) found for those wavelengths. However, as further discussed in the next section, and displayed in Figure 16, the values of the slopes thus obtained are fully compatible with those used by Désert et al. (1990) based in part on IRAS data, and those computed by Boulanger et al. (1996) based on COBE/DIRBE and FIRAS data .

6. Discussion

On the one hand, Figure 16 provides a summary of all the measurements performed in this paper. We also superpose data from the literature as indicated. Péault et al. (1991) provides a cosecant measurement in the UV of the diffuse component. Interestingly, it confirms that it does not have a substantial contribution. On the other hand, Table 6 gives numerical values of the surface brightness for UBVRI filters and a comparison with other works. Table 7 summarises similarly the values for near-infrared and infrared.

We have shown with simulations that the surface brightness of the Galaxy at the Solar Neighbourhood as observed from outside the Galaxy can be computed with a cosecant averaging of all-sky surveys. While face-on estimates performed on external galaxies are not very sensitive to extinction, our measurements severely suffer from extinction due to our internal view

point. We have computed the extinction corrections necessary to apply to the direct cosecant averaging estimates. Relying on these results, we compute synthetic spectral estimates of the optical surface brightness. We use the Hipparcos catalogue and the Hipparcos Input Catalogue together with a stellar spectral flux library to estimate the expected contribution of stars in the optical. We use the knowledge of the stellar parallaxes and of the completeness limit to perform this estimate. We attempt to correct the incompleteness (uncertain parallaxes and stars below the completion limits) with corrections based on our simulations. We then compile optical and infra-red sky-surveys to obtain direct observational estimates.

We observe a systematic difference between our synthetic estimates and the optical and infra-red sky-surveys. The estimate based on USNO-A2 R flux in the magnitude range $12 \leq R < 18$ exhibits a large excess with respect to our simulations. This excess is compatible with the disagreement observed between Pioneer 10/11 and our synthetic estimates. On the other hand, in the B band the TYCHO and USNO-A2 data are in relatively good agreement with the simulations and with our synthetic estimate. The Pioneer 10/11 estimate nevertheless exhibits an excess (similar to what is observed in R). Various arguments could be evoked to provide tentative explanations for these differences:

- The USNO-A2 data exhibit a very irregular pattern in B, which is not observed in R. This might be an indication of patchy absorption affecting solely the B data. Patchy extinction is not included in our simulations nor in the extinction correction. However, we would expect the Pioneer 10/11 data to be affected the same way. There might be some other not understood problem with the B data.
- The synthetic estimates are based on the Hipparcos data only (distance limited sample with $V < 7.3$), while the all-sky surveys integrate the whole sky. In practice, the all-sky surveys probe an equivalent cylinder radius of 1 kpc, while the synthetic estimates are based on the Hipparcos data complete within $\sim 100\text{-}200\text{ pc}$ depending on the magnitude range. In order to provide a surface brightness estimate within 1 kpc, we have applied appropriate corrections. However, these corrections are normalised to the local stellar density measured by Hipparcos and assume a uniform stellar density following the exponential disc geometry. We suggest that this disagreement could be a signature of the presence of the local minimum of the stellar density linked with Gould’s belt. As displayed in Fig. D.3, the magnitude interval $10 \leq V < 18$ is roughly composed of $\langle M_V \rangle = 4 - 5$ stars. In addition, we know that the strongest contribution comes from $-3 < M_V < 6$ (see Fig. D.2). The irregular distribution of OB stars (not accounted for in our correction for synthetic estimates, nor in our modelling) plays an important role.
- The all-sky surveys estimates follow the same profile as the synthetic estimates. This is also compatible with a minimum of the stellar density (the bright stars are the main contributors to the surface brightness).
- The Pioneer 10/11 data points, when uncorrected for extinction, are in good agreement with our synthetic esti-

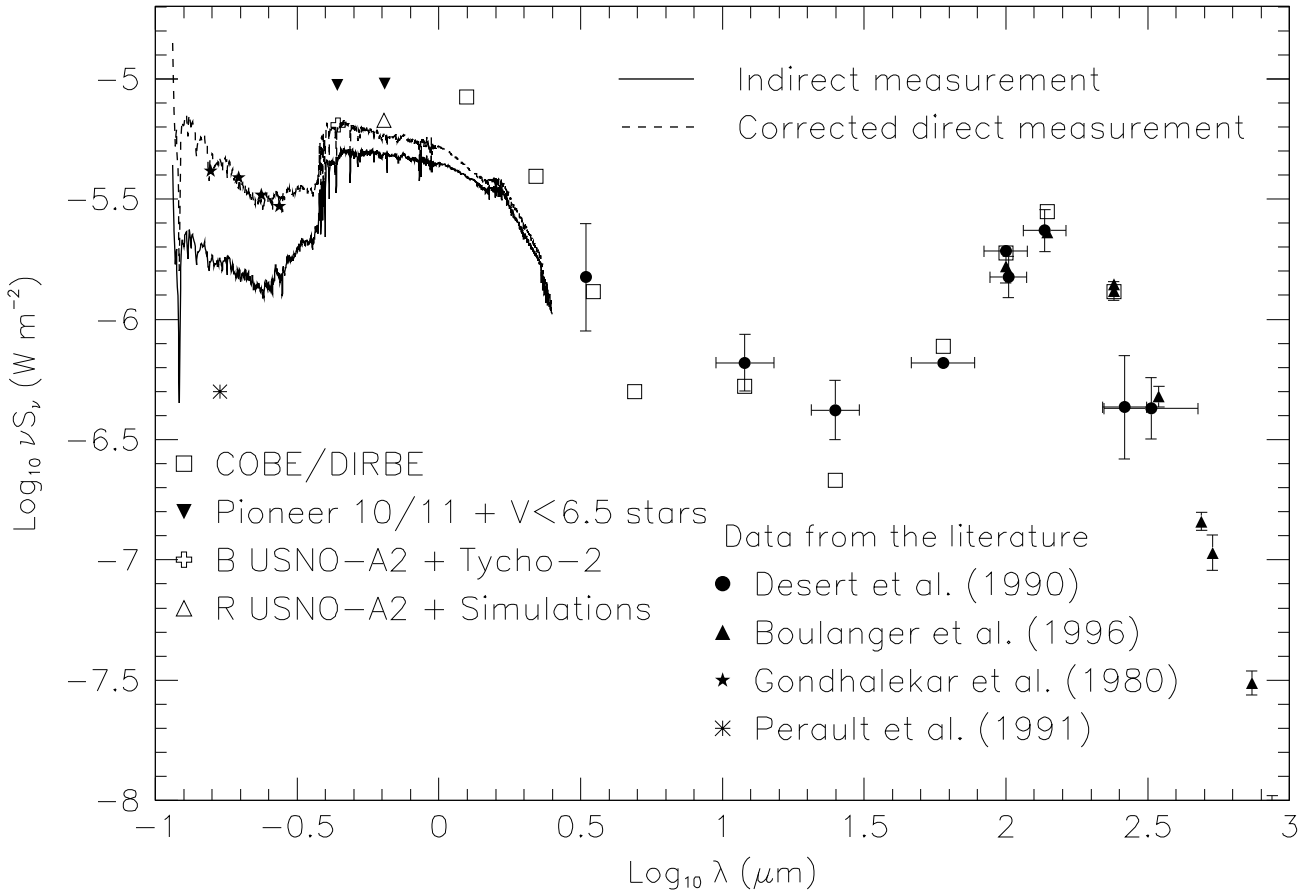


Fig. 16. Summary of the measurements discussed throughout this paper. The data points with no error bars have been computed with the cosecant law extrapolation method applied at given wavelengths (COBE/DIRBE, Pioneer 10/11, USNO-A2 & Tycho-2). The Pioneer 10/11 and COBE/DIRBE 1.25 μm and 2.2 μm are corrected for extinction (cf. Table E.1) by the amount indicated by the vertical lines attached to the Pioneer 10/11 points. In parallel, the *dashed* and *full line* curves correspond to the stellar synthetic estimates based on Hipparcos data. In the IR, our estimates based on COBE/DIRBE are compatible with Désert et al. (1990), Boulanger et al. (1996) (symbols with error bars). As discussed in § 5, the 12 μm and 25 μm data points are probably affected by uncertainties due to Zodiacal light residuals. In the UV, the uncertainties are large due to the sensitivity to inhomogeneities (OB associations). Our indirect estimate is compatible with the all-sky average performed by Gondhalekar et al. (1980).

mate. However, they seem at odds with respect to the DIRBE/COBE J and K data. This is difficult to understand as the synthetic estimates are corrected for extinction (star by star).

The recent work of Flynn et al. (2006) based on (partly) different data sets and a careful modelling exhibits similar trends. Their Tuorla study (which results are quoted in Tab. 6) probes stars out to circa 200 pc. Their B and V estimates are consistent with our corrected direct synthetic estimates, since the volume probed with the Hipparcos data is similar. In parallel, their I-band estimate is systematically larger than our synthetic estimate and closer to our Pioneer 10/11 estimates. This is in agreement with our Gould's belt interpretation as I-band surface brightness should be less sensitive to inhomogeneities, and suggests that our incompleteness correction, assuming homogeneity of the stellar distribution (see Eq. 7), probably misses some stars in I. Our results could explain why Flynn et al. (2006) find that the global luminosity of the Milky Way appears to be under-luminous with respect to the

main locus of the Tully-Fisher relation as observed for external galaxies.

We thus conclude that the presence of Gould's belt affects our measurements of the surface brightness of the Galaxy at the Solar Neighbourhood. All-sky surveys (Pioneer 10/11 and DIRBE/COBE) do not suffer from magnitude limits and enable to probe the whole volume expected. Our synthetic estimates based on Hipparcos data underestimate the surface brightness by a factor about 2. We tentatively interpret this difference as a signature of Gould's belt. The stellar catalogues tend partially to support this interpretation. In the R band, we observed an excess in the USNO-A2 data compatible with the Pioneer 10/11 estimate.

Acknowledgements. We thank G. Lagache for her efficient help for the COBE/DIRBE data handling, R. Drimmel for providing an adapted version of his published J,K model, and A. Robin for providing us simulations prior to their publication. We are most grateful to K. Gordon and his collaborators for providing their Pioneer 10/11 data, which have been very valuable for this study. We thank Guy Simon for preparing an adapted catalogue from the DENIS database.

Table 6. Summary for surface brightness measurements for the usual optical bands and comparison with other estimates. The various estimates discussed in this paper have been gathered and provided in the different usual units. As discussed in the text, the values obtained for Pioneer 10/11, probing a larger volume than the (corrected estimate) synthetic estimate based on the Hipparcos data, are systematically larger (brighter). Our (corrected direct) synthetic estimate is compatible with the Flynn et al. (2006) data in B and V. In the I band, the Flynn et al. (2006) estimate is between our synthetic and Pioneer 10/11 estimates. This could be a bias of our incompleteness correction, used for synthetic estimates, based on V data, which assumes homogeneity of the stellar distribution. However, the Pioneer data (supported by the COBE/DIRBE near-infrared) estimates suggest that the surface brightness of the Milky Way is brighter. This could explain why Flynn et al. (2006) observed that the Milky Way appears to be underluminous with respect to the main locus of the Tully-Fisher relation for external galaxies.

λ c_λ $L_\odot^\lambda = \lambda F_\odot^\lambda$	Unit W m^{-2} $\text{L}_\odot \text{ pc}^{-2}$	U 3660 1.48×10^{-8} 0.282	B 4400 2.90×10^{-8} 0.558	V 5530 1.97×10^{-8} 0.745	R_C 6400 1.44×10^{-8} 0.753	R_J 6930 1.25×10^{-8} 0.737	I_C 7900 9.66×10^{-9} 0.661	I_J 8785 7.77×10^{-9} 0.622
This paper								
Synthetic estimates								
- corrected direct	10^{-6} W m^{-2} $\text{L}_\odot \text{ pc}^{-2}$ $\text{L}_\odot^\lambda \text{ pc}^{-2}$ mag/''	3.662 9.08 32.20 23.34	6.249 15.49 27.76 23.49	6.081 15.07 20.23 23.10	5.848 14.50 19.26 22.80	5.758 14.27 19.36 22.66	5.46 13.56 20.51 22.44	5.347 13.25 21.30 22.23
- indirect	10^{-6} W m^{-2} $\text{L}_\odot \text{ pc}^{-2}$ $\text{L}_\odot^\lambda \text{ pc}^{-2}$ mag/''	2.433 6.03 21.38 23.78	4.618 11.45 20.52 23.81	4.924 12.21 16.39 23.33	4.864 12.06 16.36 23.00	4.817 11.94 16.20 22.86	4.597 11.40 17.25 22.63	4.495 11.14 17.91 22.41
USNO-A2	10^{-6} W m^{-2} $\text{L}_\odot \text{ pc}^{-2}$ $\text{L}_\odot^\lambda \text{ pc}^{-2}$ mag/''		6.13 15.19 27.23 23.51		6.71 16.63 22.08 22.6			
Pioneer 10/11 ^a	10^{-6} W m^{-2} $\text{L}_\odot \text{ pc}^{-2}$ $\text{L}_\odot^\lambda \text{ pc}^{-2}$ mag/''	(6.23) (15.44) (54.76) (22.76)	8.98 22.26 39.89 23.09	(10.34) (25.63) (34.41) (22.52)	9.54 23.65 (31.41) 22.27	(9.79) (24.27) (32.93) (22.09)	(9.30) (23.05) (34.87) (21.86)	(9.51) (23.58) (37.90) (21.60)
Basic simulations	10^{-6} W m^{-2} $\text{L}_\odot \text{ pc}^{-2}$ $\text{L}_\odot^\lambda \text{ pc}^{-2}$ mag/''		5.13 12.72 22.79 23.67	4.23 10.51 14.11 23.49	4.76 11.81 15.68 23.02			
Comparison with other works^b								
v. der Kruit (1986)	10^{-6} W m^{-2} $\text{L}_\odot \text{ pc}^{-2}$ $\text{L}_\odot^\lambda \text{ pc}^{-2}$ mag/''		4.68 11.61 20.81 23.8					
Flynn et al. (2006)	10^{-6} W m^{-2} $\text{L}_\odot \text{ pc}^{-2}$ $\text{L}_\odot^\lambda \text{ pc}^{-2}$ mag/''		6.12 15.16 27.70 23.51	7.09 17.57 23.59 22.93		7.96 19.74 29.86 22.03		

^a Values provided in parenthesis have been obtained as an interpolation based on the corrected direct template adjusted on the Pioneer 10/11 and COBE/DIRBE measurements (factor 1.7).

^b The surface brightness measurements in W m^{-2} , $\text{L}_\odot \text{ pc}^{-2}$ and $\text{L}_\odot^\lambda \text{ pc}^{-2}$ provided for the estimates of van der Kruit (1986) and Flynn et al. (2006) have been derived with the calibration constants c_λ and L_\odot^λ provided on the top of this table and computed with Eq. B.2. These $\text{L}_\odot^\lambda \text{ pc}^{-2}$ values are compatible with the original values within 10% uncertainties, due to the difference of L_\odot^λ solar luminosity considered.

We also acknowledge useful discussions with J. Guibert and M. Péault at various stages of this work. Work by AG was supported by grant AST 0452758 from the US NSF. ALM has been supported during part of this work by a grant from the Société de Secours des Amis des Sciences. This research has made use of the NASA/IPAC Extragalactic Database (NED), which is operated by the Jet Propulsion Laboratory, California Institute of Technology, under contract with the National Aeronautics and Space Administration.

References

- Allen, C. W. 1973, *Astrophysical Quantities* (London: Athlone Press)
- Arendt, R. G. et al. 1998, *ApJ*, 508, 74 astro-ph/9805323
- Arenou, F., Grenon, M., & Gómez, A. 1992, *A&A*, 258, 104
- Berghöfer, T. W. & Breitschwerdt, D. 2002, *A&A*, 390, 299
- Boulanger, F., Abergel, A., Bernard, J.-P., Burton, W. B., Désert, F.-X., Hartmann, D., Lagache, G., & Puget, J.-L.

Table 7. Summary for surface brightness measurement in the near-infrared and in the infrared comparison with previous measurements. Our measurements are compatible with those of Désert et al. (1990). Both are systematically larger than our synthetic estimates based on the V luminosity function, corrected for incompleteness assuming a homogeneous stellar density.

λ	Unit μm	J 1.25	K 2.20	L 3.50	4.90	12	25	60	100	140	240
This paper											
DIRBE	10^{-6} W m^{-2}	7.50	3.74	1.31	0.50	0.53	0.21	0.77	1.88	2.81	1.30
Synthetic estimates											
- corrected direct	10^{-6} W m^{-2}	4.30	2.00								
- indirect	10^{-6} W m^{-2}	3.92	1.85								
Previous works											
		$3.3\mu\text{m}$									
Désert et al. (1990) ^a	10^{-6} W m^{-2}	1.5 ± 0.8		0.66 ± 0.18		0.42 ± 0.12		0.66 ± 0.04		1.92 ± 0.07	

^a We assume a column density of hydrogen $N_H = 3 \times 10^{20} \text{ cm}^{-2}$.

1996, *A&A*, 312, 256
 Boulanger, F. & Pérault, M. 1988, *A&A*, 330, 964
 Bucciarelli, B., et al. 2001, *A&A*, 368, 335
 Burton, W. B. & Te Lintel Hekkert, P. 1986, *A&AS*, 65, 427
 Cambrésy, L., Reach, W. T., Beichman, C. A., & Jarrett, T. H. 2001, *ApJ*, 555, 563
 Dale, D. A., Helou, G., Contursi, A., Silbermann, N. A., & Kolhatkar, S. 2001, *ApJ*, 549, 215
 Désert, F., Boulanger, F., & Puget, J.-L. 1990, *A&A*, 237, 215
 de Zeeuw, P. T., Hoogerwerf, R., de Bruijne, J. H. J., Brown, A. G. A., & Blaauw, A. 1999, *AJ*, 117, 354
 Drimmel, R. & Spergel, D. N. 2001, *ApJ*, 556, 181
 Drimmel, R., Cabrera-Lavers, A., & López-Corredoira, M. 2003, *A&A*, 409, 205
 Dwek, E. et al. 1997, *ApJ*, 475, 565
 Fioc, M. & Rocca-Volmerange, B. 1997, *A&A*, 326, 950
 Fitzpatrick, E. L. 1999, *PASP*, 111, 63
 Fouqué, P. et al. 2000, *A&AS*, 141, 313
 Flynn, C., & Holmberg, J. 2003, *MNRAS*, accepted (astro-ph/0608193)
 Gispert, R., Lagache, G., & Puget, J. L. 2000, *A&A*, 360, 1
 Gondhalekar, P. M., Philips, A., & Wilson, R. 1980, *A&A*, 85, 272
 Gordon, K., Witt, A. N., & Friedmann, B. C. 1998, *ApJ*, 498, 540
 Guiderdoni, B., Hivon, E., Bouchet, F. R., & Maffei, B. 1998, *MNRAS*, 295, 877
 Hakkila, J., Myers, J. M., Stidham, B. J., & Hartmann, D. H. 1997, *AJ*, 114, 2043
 Hauser, M. G. & Dwek, E. 2001, *ARA&A*, 39, 249
 Humphreys, R. & Larsen, J. Q. 1995, *AJ*, 110, 2183
 Hayakawa, S., et al. 1981, *A&A*, 100, 116
 Henry, R. C. 2002, *A&A*, in press
 Høg, E. et al. 2000, *A&A*, 355, L27
 Jahreiss, H. & Wielen, R. 1997, in HIPPARCOS '97. Presentation of the Hipparcos and Tycho catalogs and first astrophysical results of the Hipparcos space astrometry mission, ed. B. Battrick, M.A.C. Perryman & P.L. Bernacca, 675
 Kovalevsky, J. 1998, *A&A*, 340, L35
 Kelsall, T. et al. 1998, *ApJ*, 508, 44
 Lallement, R., Welsh, B. Y., Vergely, J. L., Crifo, F., & Sfeir, D. 2003, *A&A*, 411, 447
 Lang, K., 1992, *Astrophysical Data: Planets and Stars*. (New-York: Springer-Verlag)
 Leinert, C., et al. 1998, *A&AS*, 127, 1
 Li, A. & Draine, B. T. 2001, *ApJ*, 554, 778
 Lutz, T. & Kelker, D. 1973, *PASP*, 85, 573
 Maihara, T. et al. 2001, *PASJ*, 53, 25
 Maíz-Apellániz, J. 2001, *AJ*, 121, 2742
 Mathis, J. S., Mezger, P. G., & Panagia, N. 1983, *A&A*, 128, 212
 Mattila, K. 1980b, *A&AS*, 39, 53
 —. 1980a, *A&A*, 82, 373
 Mezger, P. G., Mathis, J. S., & Panagia, N. 1982, *A&A*, 105, 372
 Miller, G. E. & Scalo, J. M. 1979, *ApJS*, 41, 513
 Monet, D. G., et al. 2003, *AJ*, 125, 984
 Monet D. et al. 1998, USNO-A V2.0, A Catalog of Astrometric Standards (U.S. Naval Observatory Flagstaff Station (USNOFS) and Universities Space Research Association (USRA) stationed at USNOFS.)
 Murthy J., & Henry, R. C. 1995, *ApJ*, 448, 848
 Pérault, M., Lequeux, J., Hanus, M., & Joubert, M. 1991, *A&A*, 246, 243
 Perryman, M., et al. 1997, *A&A*, 323, L49
 Pickles, A. J. 1998, *PASP*, 110, 863
 Poppel, W. 1997, *Fundamentals of Cosmic Physics*, 18, 1
 Reylé, C. & Robin, A. C. 2001a, *A&A*, 373, 886
 Robin, A. C., Crézé, M., & Mohan, V. 1992, *A&A*, 265, 32
 Robin, A. C., Reyle, & Crézé. 2000, *A&A*, 359, 103
 Schlegel, D. J., Finkbeiner, D. P., & Davis, M. 1998, *ApJ*, 500, 525
 Sfeir, D. M., Lallement, R., Crifo, F., & Welsh, B. Y. 1999, *A&A*, 346, 785
 Smith, H. 1987, *A&A*, 188, 233
 Toller, G., Tanabe, H., & Weinberg, J.-L. 1987, *A&A*, 188, 24
 Turon, C., et al. 1992, *A&A*, 258, 74
 Turon, C., et al. 1995, *A&A*, 304, 82
 van der Kruit, P. C. 1986, *A&A*, 157, 230

van Leeuwen, F., Evans, D. W., Grenon, M., Grossmann, V.,
Mignard, F., & Perryman, M. A. C. 1997, *A&A*, 323, 61
Vergely, J.-L., Freire Ferrero, R., Egret, D., & Köpper, J. 1998,
A&A, 340, 543
Welsh, B. Y., Sfeir, D. M., Sirk, M. M., & Lallement, R. 1999,
A&A, 352, 308
Welsh, B. Y., Sallmen, S., Sfeir, D., Shelton, R. L., &
Lallement, R. 2002, *A&A*, 394, 691
Werner, M. W. & Salpeter, W. E. 1969, *MNRAS*, 145, 249
Wicenec, A. & van Leeuwen, F. 1995, *A&A*, 304, 160
Wouterloot, J. G. A., Brand, J., Burton, W. B., & Kwee, K. K.
1990, *A&A*, 230, 21
Zacharias, N., et al. 2000, *AJ*, 120, 2131

List of the Appendices

A Tables	15
B Surface brightness definition	20
C Normalisation factor of the cosecant integration method	20
D Luminosity function (LF)	21
D.1 Uncertainties	21
D.2 Computation of the LF for direct/in direct estimates	21
D.3 3D visualisation of the Hipparcos data	22
E Extinction Modelling	22
F Comparison of the USNO-A2 with UCAC-1 data	23
G Calibration of the USNO-A2 data	24

Appendix A: Tables

Table A.1 is discussed in Sect. 2.1.3, and corresponds to Fig. 6 and 7. Table A.2 is discussed in Sect. 4.1.1 and corresponds to Fig. 10 and 11. Table A.3 is discussed in Sect. 4.1.2 and corresponds to Fig. 12. Table A.4 is discussed in Sect. 5.

Table A.1. Simulated V surface brightness (in 10^{-9} W m^{-2}) contributions obtained for each magnitude bin and sky area derived from the cosecant laws (see Fig. 6 and 7). We give the values fitted for $1/\sin |b| < 6$. The last column provides the percentages of the total surface brightness (PTSB) corresponding to each apparent magnitude bin.

Mag.	Galactic Centre				Galactic anti-centre				PTSB	
	North		South		North		South			
	($ b = 90^\circ$)	slope	($ b = 90^\circ$)	slope	($ b = 90^\circ$)	slope	($ b = 90^\circ$)	slope		
$-6. \leq V < -5.$	1.59	0.01	1.75	-0.02	1.58	0.01	1.74	-0.02	0.00	
$-5. \leq V < -4.$	3.22	0.03	3.63	-0.04	3.21	0.03	3.62	-0.05	0.00	
$-4. \leq V < -3.$	6.42	0.08	7.42	-0.10	6.40	0.08	7.40	-0.10	0.00	
$-3. \leq V < -2.$	12.38	0.19	14.58	-0.18	12.33	0.18	14.51	-0.19	0.00	
$-2. \leq V < -1.$	22.03	0.45	26.39	-0.18	21.92	0.43	26.23	-0.20	0.02	
$-1. \leq V < 0.$	33.65	0.95	41.28	0.04	33.41	0.90	40.95	-0.02	0.07	
$0. \leq V < 1.$	46.21	1.92	58.39	0.83	45.73	1.80	57.72	0.69	0.19	
$1. \leq V < 2.$	60.78	3.81	79.89	2.68	59.90	3.53	78.65	2.33	0.44	
$2. \leq V < 3.$	77.80	7.04	105.25	6.52	76.31	6.44	103.14	5.74	0.93	
$3. \leq V < 4.$	97.42	12.20	133.22	13.55	95.11	10.97	129.97	11.91	1.75	
$4. \leq V < 5.$	114.73	19.73	156.69	24.60	111.48	17.43	152.15	21.45	2.99	
$5. \leq V < 6.$	126.08	29.80	170.50	39.46	121.93	25.81	164.76	33.95	4.64	
$6. \leq V < 7.$	129.27	41.86	171.86	56.79	124.54	35.43	165.45	47.89	6.54	
$7. \leq V < 8.$	121.18	54.42	157.62	74.29	116.69	44.79	151.73	60.97	8.43	
$8. \leq V < 9.$	103.83	65.20	131.20	88.66	100.72	51.80	127.52	70.21	9.92	
$9. \leq V < 10.$	81.34	71.83	98.88	96.77	80.58	54.68	98.81	73.33	10.67	
$10. \leq V < 11.$	57.95	73.32	67.15	97.35	59.87	53.14	70.98	70.11	10.57	
$11. \leq V < 12.$	36.40	70.18	39.66	91.47	40.77	48.12	46.80	62.22	9.78	
$12. \leq V < 13.$	17.82	63.85	17.30	81.55	24.56	40.99	27.23	51.90	8.57	
$13. \leq V < 14.$	3.10	55.52	0.36	69.55	12.29	32.83	12.94	40.75	7.14	
$14. \leq V < 15.$	-6.67	45.88	-10.36	56.48	4.39	24.57	4.05	29.97	5.64	
$15. \leq V < 16.$	-11.39	35.80	-15.04	43.40	0.18	17.16	-0.47	20.61	4.21	
$16. \leq V < 17.$	-12.28	26.38	-15.36	31.54	-1.42	11.17	-2.03	13.23	2.96	
$17. \leq V < 18.$	-10.73	18.32	-13.04	21.64	-1.43	6.72	-1.85	7.86	1.96	
$18. \leq V < 19.$	-7.94	11.88	-9.47	13.88	-0.82	3.74	-1.04	4.33	1.22	
$19. \leq V < 20.$	-5.07	7.21	-5.96	8.34	-0.34	2.00	-0.42	2.29	0.71	
$20. \leq V < 21.$	-2.99	4.23	-3.47	4.84	-0.15	1.09	-0.18	1.24	0.41	
$21. \leq V < 22.$	-1.82	2.51	-2.08	2.85	-0.12	0.62	-0.14	0.70	0.24	
$22. \leq V < 23.$	-1.19	1.51	-1.34	1.71	-0.11	0.35	-0.13	0.39	0.14	
$23. \leq V < 24.$	-0.77	0.89	-0.87	1.00	-0.09	0.19	-0.10	0.21	0.08	
$24. \leq V < 25.$	-0.46	0.49	-0.52	0.55	-0.05	0.09	-0.06	0.10	0.04	
$25. \leq V < 26.$	-0.25	0.24	-0.28	0.27	-0.03	0.04	-0.03	0.05	0.02	
$26. \leq V < 27.$	-0.12	0.11	-0.13	0.12	-0.01	0.02	-0.01	0.02	0.01	
$27. \leq V < 28.$	-0.05	0.04	-0.05	0.05	0.00	0.01	-0.01	0.01	0.00	
$28. \leq V < 29.$	-0.02	0.02	-0.02	0.02	0.00	0.00	0.00	0.00	0.00	
$29. \leq V < 30.$	-0.01	0.01	-0.01	0.01	0.00	0.00	0.00	0.00	0.00	

Direct sum									
$V < 0$	79.28	1.71	95.05	-0.48	78.83	1.63	94.46	-0.57	
$0 \leq V < 7$	652.30	116.36	875.80	144.44	635.00	101.41	851.85	123.96	
$7 \leq V < 11$	364.30	264.78	454.84	357.07	357.86	204.42	449.04	274.62	
$11 \leq V < 20$	3.24	335.03	-11.90	417.84	78.18	187.29	85.21	233.17	
$20 \leq V < 30$	-7.67	10.04	-8.77	11.42	-0.57	2.41	-0.66	2.72	
Total	1091.45	727.92	1405.03	930.29	1149.30	497.15	1479.90	633.90	

Total value: 5126 ($ b = 90^\circ$), 2789 (slope)

Table A.2. Contributions from TYCHO-2 and USNO-A2 stars to the B surface brightness, given in 10^{-9} W m^{-2} . We give the values fitted to TYCHO-2 and USNO-A2 B data (see Figs. 10 and 11) for each sky area and magnitude bin. We also provide the corresponding values obtained with simulations.

B mag.	Galactic Centre				Galactic Anti-Centre			
	North		South		North		South	
Test	$ b = 90^\circ$	slope	$ b = 90^\circ$	slope	$ b = 90^\circ$	slope	$ b = 90^\circ$	slope
TYCHO-2 data								
$6 \leq B < 7$	117.26	42.60	127.84	44.63	156.98	18.52	148.84	52.60
$7 \leq B < 8$	144.37	36.62	143.04	45.85	154.85	34.38	157.57	53.65
$8 \leq B < 9$	134.97	46.45	150.55	55.16	166.30	41.65	156.32	54.84
$9 \leq B < 10$	147.35	47.23	151.01	64.20	164.94	50.75	158.00	56.83
$10 \leq B < 11$	143.05	53.38	154.52	69.20	156.43	56.14	151.58	53.71
USNO-A2 data								
$12 \leq B < 13$	98.71	71.33	172.82	60.27	105.69	56.87	129.03	46.31
$13 \leq B < 14$	66.24	64.01	88.08	80.64	85.80	49.79	93.22	41.05
$14 \leq B < 15$	44.11	61.04	36.34	95.43	60.89	45.45	60.29	40.86
$15 \leq B < 16$	24.81	59.49	2.90	102.94	43.99	40.07	34.36	39.84
$16 \leq B < 17$	10.97	54.41	-12.62	97.11	23.10	33.13	16.33	33.32
$17 \leq B < 18$	-2.58	49.07	-15.81	79.41	7.92	24.74	6.19	24.73
$18 \leq B < 19$	-5.50	36.95	-11.52	58.80	3.29	13.60	0.43	15.43
Simulations								
$6. \leq B < 7.$	134.14	36.53	177.34	49.10	129.41	30.81	170.95	41.20
$7. \leq B < 8.$	132.53	46.41	171.57	62.97	127.44	38.26	164.90	51.72
$8. \leq B < 9.$	122.53	55.15	154.82	74.66	117.63	44.19	148.74	59.60
$9. \leq B < 10.$	105.65	61.44	129.94	82.38	101.49	47.55	125.28	63.46
$10. \leq B < 11.$	83.91	64.51	100.27	85.24	80.90	47.96	97.53	62.99
$11. \leq B < 12.$	59.73	64.27	69.13	83.45	58.41	45.54	68.77	58.72
$12. \leq B < 13.$	35.89	61.02	39.71	77.81	37.20	40.65	42.65	51.44
$13. \leq B < 14.$	15.42	55.09	15.26	69.05	20.32	33.80	22.46	42.04
$14. \leq B < 15.$	0.95	46.83	-1.46	57.79	9.22	25.94	9.60	31.74
$15. \leq B < 16.$	-6.86	37.20	-9.94	45.23	3.09	18.39	2.81	22.17
$16. \leq B < 17.$	-9.61	27.73	-12.42	33.25	0.16	12.20	-0.27	14.49
$17. \leq B < 18.$	-9.52	19.62	-11.73	23.22	-0.95	7.62	-1.33	8.94
$18. \leq B < 19.$	-8.03	13.22	-9.62	15.47	-1.05	4.46	-1.31	5.17
Data Sums								
$6 \leq B < 11$	687.00	226.28	772.31	271.63	799.50	201.44	726.96	279.04
$12 \leq B < 19$	236.76	396.30	260.19	574.60	330.68	263.65	339.85	241.54
Simulated Sums								
$6 \leq B < 11$	578.76	264.03	733.94	354.35	556.88	208.77	707.41	278.97
$12 \leq B < 19$	18.24	260.71	9.79	321.82	67.99	143.07	74.60	175.99
Total contributions								
Data								
$ b = 90^\circ$				slope		$ b = 90^\circ$		slope
$-6 \leq B < 6$								295.43
$6 \leq B < 11$	2985.77			978.39			2577.02	1106.12
$11 \leq B < 12$	(98.44)			(225.75)			256.04	251.98
$12 \leq B < 19$	1167.48			1476.09			170.62	901.59
$6 \leq B < 19$	4163.			2680.			5845.42.	2555.12
$6 \leq B < 11$ and $12 \leq B < 19$	4153.			2454.			5845.42.	2555.12
$6 \leq B < 19$	(7251.)			(3004.)			5845.42.	2555.12

Table A.3. USNO-A2 R fluxes, given in 10^{-9} W m^{-2} . We give the values fitted to USNO-A2 R fluxes (see Fig. 12) for $1/\sin(b) < 6$.

R mag.	Galactic Centre				Galactic Anti-Centre				
	North		South		North		South		
	$ b = 90^\circ$	slope	$ b = 90^\circ$	slope	$ b = 90^\circ$	slope	$ b = 90^\circ$	slope	
USNO-A2 data									
$12 \leq R < 13$	79.69	145.06	100.21	202.54	92.32	95.03	94.15	84.65	
$13 \leq R < 14$	37.06	150.61	4.46	244.76	64.51	89.38	86.42	74.08	
$14 \leq R < 15$	13.02	129.08	-38.66	212.66	48.15	71.91	41.65	68.61	
$15 \leq R < 16$	1.80	110.32	-53.84	182.94	26.44	61.73	22.37	56.58	
$16 \leq R < 17$	-8.92	88.87	-48.69	143.69	8.12	43.45	7.76	40.04	
$17 \leq R < 18$	-14.86	77.51	-47.94	121.75	-1.23	30.52	1.66	29.04	
Simulations									
$-6 \leq R < -5$	2.24	0.02	2.47	-0.02	2.24	0.02	2.47	-0.03	
$-5 \leq R < -4$	4.19	0.04	4.62	-0.04	4.18	0.03	4.61	-0.05	
$-4 \leq R < -3$	8.03	0.08	9.06	-0.11	8.01	0.08	9.04	-0.11	
$-3 \leq R < -2$	16.20	0.22	18.77	-0.25	16.15	0.21	18.70	-0.25	
$-2 \leq R < -1$	25.31	0.43	30.31	-0.39	25.19	0.42	30.15	-0.40	
$-1 \leq R < 0$	37.62	1.02	46.91	-0.24	37.36	0.98	46.55	-0.28	
$0 \leq R < 1$	51.95	2.17	67.20	0.69	51.40	2.05	66.43	0.56	
$1 \leq R < 2$	68.12	4.62	91.55	3.37	67.05	4.32	90.05	3.00	
$2 \leq R < 3$	88.53	8.91	121.29	8.90	86.63	8.22	118.61	8.00	
$3 \leq R < 4$	107.01	16.05	147.62	19.07	104.05	14.53	143.44	17.01	
$4 \leq R < 5$	120.52	26.40	165.66	34.26	116.51	23.33	160.06	30.03	
$5 \leq R < 6$	124.63	39.66	169.40	53.60	120.13	34.08	163.17	45.86	
$6 \leq R < 7$	117.68	54.20	157.03	74.33	113.76	45.12	151.73	61.71	
$7 \leq R < 8$	99.92	67.51	129.94	92.73	97.98	54.22	127.56	74.30	
$8 \leq R < 9$	76.71	76.42	95.67	104.57	77.90	58.91	97.90	80.35	
$9 \leq R < 10$	53.41	79.19	62.59	107.30	58.05	58.28	69.87	78.60	
$10 \leq R < 11$	33.95	75.96	36.46	101.35	41.17	53.22	47.42	70.51	
$11 \leq R < 12$	18.59	68.85	17.45	90.00	27.17	45.78	30.11	59.31	
$12 \leq R < 13$	6.01	60.16	3.06	76.90	15.59	37.60	16.55	47.60	
$13 \leq R < 14$	-3.99	50.96	-7.85	63.78	6.85	29.40	6.65	36.45	
$14 \leq R < 15$	-10.34	41.37	-14.40	50.85	1.42	21.62	0.72	26.33	
$15 \leq R < 16$	-12.74	31.82	-16.40	38.51	-1.06	14.82	-1.81	17.77	
$16 \leq R < 17$	-12.02	23.04	-14.90	27.50	-1.50	9.41	-2.06	11.13	
$17 \leq R < 18$	-9.47	15.63	-11.47	18.43	-0.99	5.55	-1.30	6.48	
$18 \leq R < 19$	-6.46	9.99	-7.69	11.64	-0.42	3.13	-0.55	3.61	
$19 \leq R < 20$	-4.04	6.16	-4.73	7.11	-0.18	1.78	-0.22	2.03	
$20 \leq R < 21$	-2.58	3.83	-2.98	4.37	-0.17	1.05	-0.20	1.19	
$21 \leq R < 22$	-1.81	2.45	-2.06	2.77	-0.19	0.62	-0.22	0.71	
Data sums									
$12 \leq R < 18$	107.79	701.45	-84.46	1108.34	238.31	392.02	254.01	353.00	
Simulated sums									
$-6 \leq R < 6$	654.35	99.62	874.86	118.84	638.89	88.26	853.29	103.34	
$6 \leq R < 12$	400.26	422.13	499.16	570.30	416.02	315.53	524.58	424.79	
$12 \leq R < 18$	-42.56	222.99	-61.97	275.96	20.31	118.39	18.74	145.75	
$18 \leq R < 22$	-14.88	22.43	-17.46	25.90	-0.96	6.58	-1.19	7.54	
Total contributions									
Data				Simulations					
$ b = 90^\circ$		slope		$ b = 90^\circ$		slope			
$-6 \leq R < 6$						3021.39		410.06	
$6 \leq R < 12$						1840.02		1732.75	
$12 \leq R < 18$	515.65		2554.81			-65.48		763.09	
$18 \leq R < 22$						-34.49		62.45	
$6 \leq R < 22$						4761.44		2968.55	

Table A.4. Values of the surface brightness computed with the COBE/DIRBE data, given in 10^{-9} W m^{-2} . We give the values fitted to the COBE/DIRBE data for $1/\sin|b| < 6$. The influence of the point sources is removed with a 5σ clipping. The slopes are computed as explained for the optical (for $1/\sin|b| < 6$), except for the 12 and 25 μm data. As explained in the text (§ 5), these data exhibit a “non-Galactic behaviour” and the corresponding fits are performed for $2 < 1/\sin|b| < 6$.

λ	Galactic Centre				Galactic Anti-Centre			
	North		South		North		South	
	$ b = 90^\circ$	slope	$ b = 90^\circ$	slope	$ b = 90^\circ$	slope	$ b = 90^\circ$	slope
1.25 μm	2050.	2240.	1720.	2790.	2180.	1130.	2320.	1330.
2.20 μm	964.	1130.	787.	1390.	1020.	541.	1050.	676.
3.50 μm	397.	393.	333.	472.	408.	191.	417.	252.
4.90 μm	324.	155.	305.	171.	317.	77.8	345.	97.3
12 μm	1630.	121.	1500.	86.7	979.	181.	1440.	139.
25 μm	1260.	57.5	1260.	28.5	1020.	69.1	1160.	59.0
60 μm	288.	239.	136.	203.	148.	133.	272.	201.
100 μm	665.	549.	406.	439.	235.	385.	563.	511.
140 μm	764.	800.	553.	567.	185.	638.	660.	802.
240 μm	315.	351.	267.	238.	45.8	332.	302.	382.

Contribution from the Galactic Centre (left) and Anti-Centre (right)

1.25 μm	3782. ($ b = 90^\circ$) 5040. (slope)	4500. ($ b = 90^\circ$) 2462. (slope)
2.20 μm	1752. ($ b = 90^\circ$) 2520. (slope)	2066. ($ b = 90^\circ$) 1216. (slope)
3.50 μm	730. ($ b = 90^\circ$) 864. (slope)	826. ($ b = 90^\circ$) 442. (slope)
4.90 μm	630. ($ b = 90^\circ$) 324. (slope)	662. ($ b = 90^\circ$) 174. (slope)
12 μm	3126. ($ b = 90^\circ$) 208. (slope)	2418. ($ b = 90^\circ$) 320. (slope)
25 μm	2522. ($ b = 90^\circ$) 86. (slope)	2182. ($ b = 90^\circ$) 128. (slope)
60 μm	424. ($ b = 90^\circ$) 442. (slope)	420. ($ b = 90^\circ$) 332. (slope)
100 μm	1070. ($ b = 90^\circ$) 988. (slope)	800. ($ b = 90^\circ$) 894. (slope)
140 μm	1318. ($ b = 90^\circ$) 1366. (slope)	844. ($ b = 90^\circ$) 1440. (slope)
240 μm	584. ($ b = 90^\circ$) 590. (slope)	246. ($ b = 90^\circ$) 714. (slope)

Surface brightness computed over the whole sky

1.25 μm	8282. ($ b = 90^\circ$) 7502. (slope)
2.20 μm	3818. ($ b = 90^\circ$) 3736. (slope)
3.50 μm	1556. ($ b = 90^\circ$) 1306. (slope)
4.90 μm	1292. ($ b = 90^\circ$) 500. (slope)
12 μm	5544. ($ b = 90^\circ$) 528. (slope)
25 μm	4704. ($ b = 90^\circ$) 214. (slope)
60 μm	844. ($ b = 90^\circ$) 774. (slope)
100 μm	1870. ($ b = 90^\circ$) 1882. (slope)
140 μm	2162. ($ b = 90^\circ$) 2806. (slope)
240 μm	930. ($ b = 90^\circ$) 1304. (slope)

Appendix B: Surface brightness definition

where R is the radius (in m) of the area probed and L_λ its luminosity in W at the wavelength λ . νS_ν can be directly transformed in $L_{\lambda\odot} \text{ pc}^{-2}$. It can also be transformed in a magnitude scale μ (mag.arcsec $^{-2}$) with:

$$\mu_\lambda = -2.5 \log_{10}[\nu S_\nu \times \frac{1}{c_\lambda} \times \frac{x_{\text{sr} \rightarrow \text{arcsec}^2}}{4\pi}] \quad (\text{B.2})$$

where $x_{\text{sr} \rightarrow \text{arcsec}^2} = 23.5 \times 10^{-12} \text{ arcsec}^2/\text{sr}$ is the solid angle normalisation. c_λ is the conversion factor of the observed surface brightness into magnitude. This conversion factor is for instance provided by NED⁵. For B, V and R bands, we thus have the following conversions:

Following the usual conventions, the surface brightness νS_ν is defined as:

$$\mu_B = -2.5 \log_{10}[\nu_B S_B \times \frac{1}{2.90 \times 10^{-8}} \times \frac{23.5 \times 10^{-12}}{4\pi}] \quad (\text{B.3})$$

$$\mu_V = -2.5 \log_{10}[\nu_V S_V \times \frac{1}{1.97 \times 10^{-8}} \times \frac{23.5 \times 10^{-12}}{4\pi}] \quad (\text{B.4})$$

$$\mu_R = -2.5 \log_{10}[\nu_R S_R \times \frac{1}{1.44 \times 10^{-8}} \times \frac{23.5 \times 10^{-12}}{4\pi}] \quad (\text{B.5})$$

with $\nu_B S_B$, $\nu_V S_V$ and $\nu_R S_R$ the surface brightness in B, V and R in W m^{-2} , while μ_B , μ_V and μ_R are in B mag arcsec $^{-2}$, V mag arcsec $^{-2}$ and R mag arcsec $^{-2}$.

Appendix C: Normalisation factor of the cosecant integration method

We check in the simple case of a uniform distribution ($n(r, b, l, M_V) = 1$, $f(A_V(r, b)) = 1$ and $\phi(M_V)L(M_V) = 1$) the normalisation of the cosecant integration method with respect to the integration in a cylinder.

$$S'_{\text{cyl}} = \left[\int_{R=0}^{R_{\text{cyl}}} \int_{z=-z_{\text{max}}}^{+z_{\text{max}}} \int_{l=0}^{2\pi} dldzR dR \right] / \pi R_{\text{cyl}}^2 = 2z_{\text{max}} \quad (\text{C.1})$$

$$S'_{\text{cosec}} = \int_{b=-\frac{\pi}{2}}^{\frac{\pi}{2}} \int_{l=0}^{2\pi} \int_{r=0}^{r_{\text{max}}(b)} \frac{r^2 dr dl \cos b \sin |b| db}{4\pi r^2} \quad (\text{C.2})$$

$$= z_{\text{max}} \quad (\text{C.3})$$

S'_{cyl} is the simplified version of the surface brightness computed as the integration in a cylinder, while S'_{cosec} corresponds to the integration with the $\sin |b|$ weighting used for the cosecant method. They differ by a factor of 2 understood as the difference of the volumes probed. As the behaviour of the exponential disc geometry is close to the plane parallel geometry (see e.g. Fig. 4), we apply this factor 2 to the normalisation of all estimates of the surface brightness based on the cosecant approximation, namely the integration in a cone (Eq. 3), the corrected direct estimate (Eqs. 6 and 7) and the cosecant compilations of the various datasets. We check that this factor does not change more than 7% with an exponential geometry.

$$\nu S_\nu = \frac{L_\lambda}{\pi R^2} \quad (\text{B.1})$$

⁵ <http://nedwww.ipac.caltech.edu/help/photoband.lst>

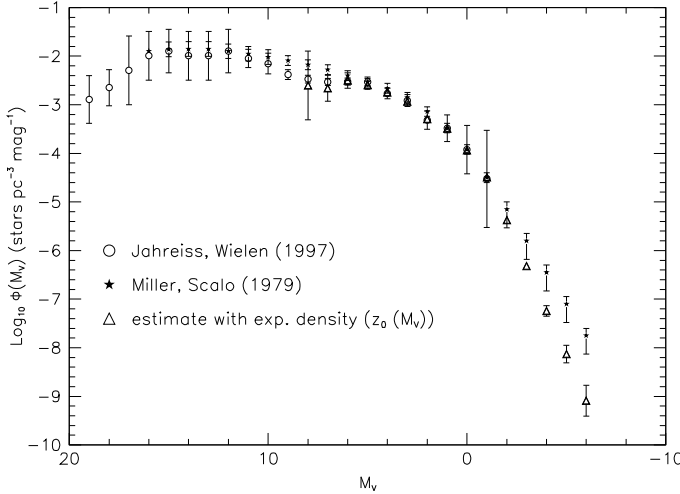


Fig. D.1. Luminosity function at the Solar Neighbourhood. The LF used for the simulation is presented (Miller & Scalo 1979; Jahreiss & Wielen 1997). The LF used for the direct/indirect estimation is also displayed with error bars accounting for Poisson noise only.

Appendix D: Luminosity function (LF)

We use two estimates of the LF to define $\phi(M_V)$: (1) the Miller & Scalo (1979) estimate for $M_V < 2$, (2) the Jahreiss & Wielen (1997) estimate based on Hipparcos data for $M_V \geq 2$. They are displayed on Fig. D.1. We find that this choice of the LF combined with the variable scale height $h_Z(M_V)$ of Miller & Scalo (1979) is equivalent to a fixed scale height $h_Z = 125\text{pc}$ (used to compare the plane parallel and exponential disc geometries).

D.1. Uncertainties

Figure D.2 shows the relative contribution to the surface brightness from the Solar Neighbourhood of each absolute-magnitude bin. This has been computed with the simulations described in Sect. 2.2. Dim stars with $M_V > 7$ do not contribute significantly to the surface brightness (1%), while the magnitude interval $-6 \leq M_V \leq 6$ is the main contributor to the surface brightness (98%). It is important to note that the bright end ($M_V < 0.5$) of the LF constitutes a significant contribution (34% of the surface brightness). Hence, theoretical estimations of the surface brightness based on the LF depend on the uncertainties on the upper tail. However, stars with $M_V < -1.5$ (resp. $M_V < -3.5$) correspond to only 11% (resp. 3%) of the surface brightness. This effect disappears when one considers stellar catalogues, which provide apparent magnitudes (see Fig. 8). Figure D.2 displays the value of the absolute magnitude of the “mean star” of each apparent magnitude bin, which gives a qualitative behaviour of these related parameters.

D.2. Computation of the LF for direct/indirect estimates

We present here the estimate of the LF, based on the Hipparcos catalogue, used to compute the direct and indirect estimates. The Hipparcos Catalogue (Perryman et al. 1997; van Leeuwen et al. 1997) is complete for $V < 7.3$, and parallaxes are available for most of the stars. We consider that the number of stars

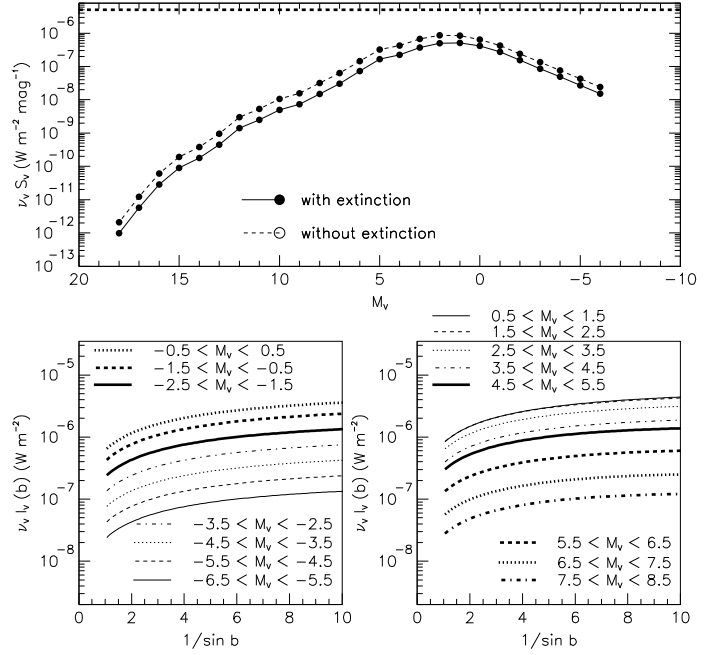


Fig. D.2. Contribution of each absolute magnitude bin to the V surface brightness (computed with $1/\sin|b| < 6$ from the Solar Neighbourhood, with $h_Z(M_V)$). The upper panel displays the contribution to $v_V S_V$ of each bin of absolute magnitude. The horizontal dashed line corresponds to the cumulated value (the estimated surface brightness). The lower panels exhibit the corresponding decomposition of $v_V I_V(|b|)$ for each absolute-magnitude bin (with extinction). These values have to be increased by 65% (see Fig. 2) to correspond to a face-on value estimate of the V surface brightness.

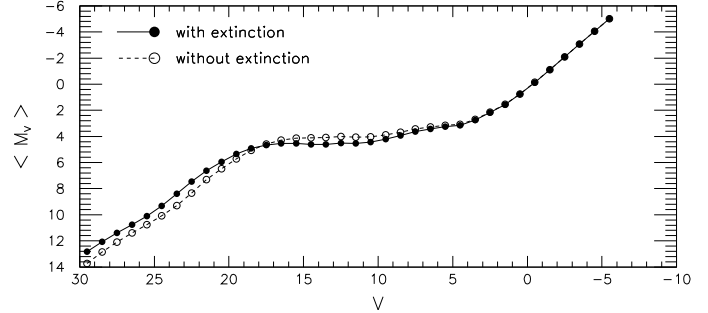


Fig. D.3. Mean absolute magnitude stars contribution to each apparent magnitude bin.

in each magnitude bin $M_V - \frac{1}{2} \leq m < M_V + \frac{1}{2}$, where m is the absolute magnitude, is complete within a sphere of radius $R(M_V + \frac{1}{2}) = 10^{(7.3-(M_V+\frac{1}{2}))/5.1+1}\text{pc}$ for $-6.5 \leq M_V < 6.5$. We count stars in these volumes $vol(R)$ using,

$$\phi(M_V) = \frac{N(M_V - \frac{1}{2} \leq m < M_V + \frac{1}{2})}{vol(R)} \quad (\text{D.1})$$

where $N(M_V - \frac{1}{2} \leq m < M_V + \frac{1}{2})$ is the number of stars found with an absolute magnitude m in this bin, and the volume is defined as: $vol(R) = \int_{r < R} \eta(r, b, l; h_Z(M_V)) r^2 d\sin b dl dr$, and where $\eta(r, b, l; h_Z(M_V)) = n(r, b, l, M_V)/n_{\odot}(M_V)$ (open triangles in Fig. D.1). This accounts for the exponential profile of the Galaxy, with different vertical scales for different magnitude ranges. We adopt the same scale heights as Miller &

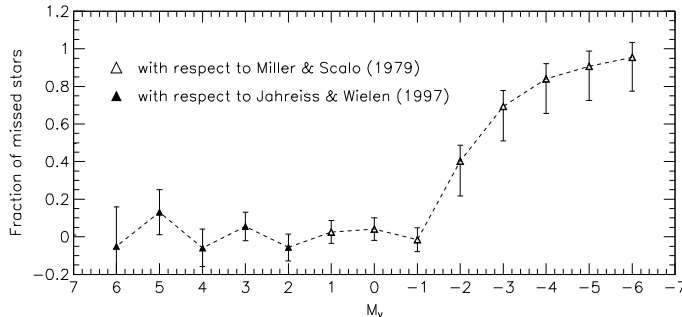


Fig. D.4. Fraction f_i^{missed} of the stars missed with respect to Miller & Scalo (1979) for each magnitude bin. The correction factor $f_i^{\text{LF}} = 1/(1 - f_i^{\text{missed}})$ is applied for the computation of the corrected and indirect estimates in Sect. 3 in order to be compatible with the simulations. The error bars account for the uncertainties on the Jahreiss & Wielen (1997); Miller & Scalo (1979) LF used for the simulations and the Poisson noise of our estimate.

Scalo (1979) ($h_Z(M_V \leq 0) = 80\text{pc}$). We also correct each star for interstellar extinction according to our extinction modelling described in Appendix E.

Among the 20 906 stars with $V < 7.3$, we consider the 18 381 stars with a parallax significant at 3σ . We further restrict this sample by 29% to account the completion limit for each magnitude bin. We then treat the 13 374 stars as follows:

- 9 444 stars have a standard spectral type with a luminosity class, that can be found in the Pickles (1998) library.
- 548 stars either have a standard spectral type with no luminosity class available in Pickles (1998) and that has to be interpolated between existing templates, or have two spectral types (the average is then adopted).
- 3 114 stars have a well defined spectral type, but no luminosity class. We rely on M_V to estimate it, and derive a template.
- 1 Wolf-Rayet star and 20 C/N stars, which do not exceed $3.06 \times 10^{-8} \text{ W m}^{-2} \text{ sr}^{-1}$ (corrected direct) and $1.40 \times 10^{-9} \text{ W m}^{-2} \text{ sr}^{-1}$ (indirect) in V.
- 247 stars, with no precise spectral type (63% Am/Ap, 18% M), are neglected. We estimate that their contribution to the V surface brightness is $6.80 \times 10^{-8} \text{ W m}^{-2} \text{ sr}^{-1}$ (corrected direct) and $5.69 \times 10^{-9} \text{ W m}^{-2} \text{ sr}^{-1}$ (indirect).

Figure D.1 summarises the LF thereby obtained. The discrepancy with respect to Miller & Scalo (1979) is significant for luminous stars. The corresponding stellar population is strongly inhomogeneous (de Zeeuw et al. 1999), and this part of the LF certainly suffers uncertainties larger than Poisson noise (see also Appendix D.3). In order, to use the same LF as for the simulations, we correct the LF as displayed in Fig. D.4, for stars brighter than magnitude -1.5 .

D.3. 3D visualisation of the Hipparcos data

We present a 3D visualisation of the Hipparcos catalogue on <http://www.ospm.fr/sbhip06>. We also position a schematic Gould's belt in the Galactic plane following Guillout et al. (1998). Gould's belt is significantly larger than the volume

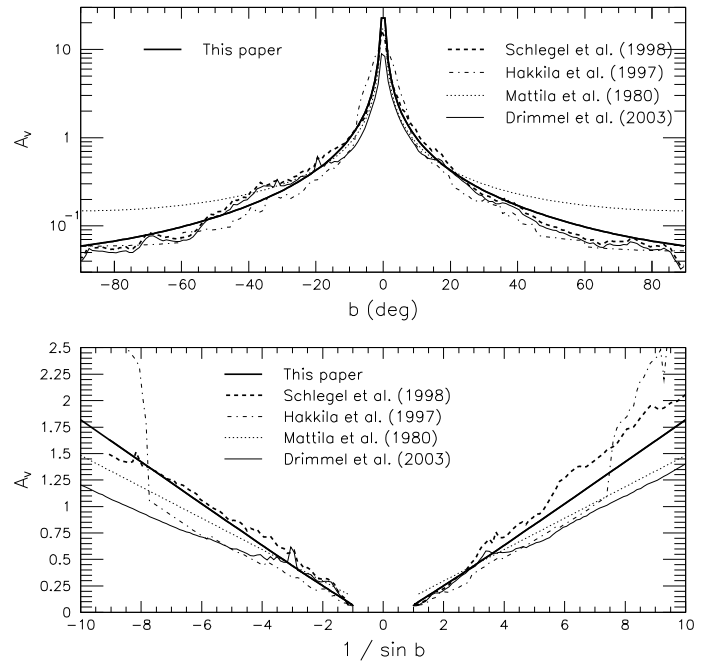


Fig. E.1. A_V extinction dependence on Galactic latitude. The extinction used for the simulations is compared with other models (Drimmel et al. 2003; Hakkila et al. 1997; Mattila 1980b) and the dust maps (Schlegel et al. 1998).

probed by the Hipparcos catalogue. The early-type stars are distributed in the Galactic Disk, but do not exhibit a clear (20deg) inclination. More generally, the Hipparcos stars distribution is clearly flatten towards the Galactic Poles, but no clear correlation with Gould's belt is detected due to the small volume sampled. For the majority of the stars, the cut in magnitude is clearly seen as a spheroidal distribution of stars. However, the bright stars exhibit a more irregular distribution. The apparent contours are roughly compatible with the local cavity observed in the gas distribution (e.g. Lallement et al. 2003), but there is not enough information to conclude about an extinction bias.

Appendix E: Extinction Modelling

In Figure E.1, we display the dependence of the A_V extinction with the Galactic latitude obtained from dust maps by Schlegel et al. (1998). We find systematic differences with Hakkila et al. (1997), based on a compilation of various models. For the purpose of this work, we wish to use a simple analytical model to describe first order effects linked to extinction. We consider the extinction model of Mattila (1980b), based on a 2-components model. Compared to the A_V extinction derived from Schlegel et al. (1998), it tends to overestimate the extinction towards the pole (even though this excess remains within the error bars quoted by Hakkila et al. 1997), and to underestimate it at intermediate latitudes. We further tune this type of law, and adopt the following empirical model:

$$A_V(r, b) = a_V \beta / \sin |b| \times \left(\frac{\pi}{b + \pi} \right)^3 \times (1 - \exp(-(r|\sin b|)/\beta)) \quad (\text{E.1})$$

Table E.1. Values of the extinction correction applied to cosecant measurements for the main filters used in this paper (see Fig. 2 and Table E.1). We consider $R_{\text{cyl}} = 1$ kpc.

λ (μm)	Correction	λ (μm)	Correction
0.44 (B)	1.72	0.69 (R_J)	1.36
0.55 (V)	1.52	1.25 (J)	1.12
0.64 (R_C)	1.41	2.20 (K)	1.05

with $a_v = 1.48$ mag/kpc and $\beta = 135$ pc. The inverse cube power of b has been defined empirically to reproduce the b dependence on Fig. E.1. This empirical law is also in good agreement with the z-dependence of the extinction modelled by Hakkila et al. (1997).

Numerical values

The extinction correction used to derive a surface brightness measurement of the Galaxy at the Solar Neighbourhood is provided in Table E.1.

Appendix F: Comparison of the USNO-A2 with UCAC-1 data

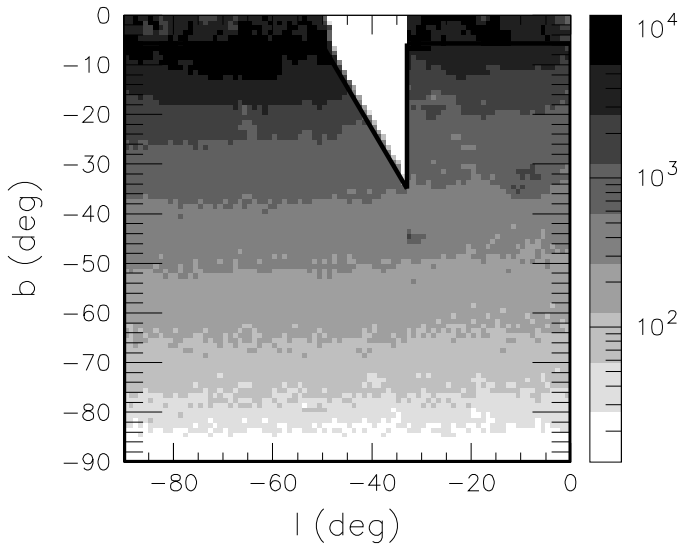


Fig. F.1. Galactic plane coverage of the UCAC-1 catalogue (Zacharias et al. 2000). We restrict our study to the area indicated with thick lines, defined by $b < 0$ and $-90^\circ < l < 0^\circ$, and we exclude the area between $l = -33^\circ$ and $b = -1.7 \times l + 522^\circ$. The intensity corresponds to the number of stars with $11 \leq R_U < 16$.

Figure F.1 displays the area of the sky considered for this comparison. Figure F.2 and Table F.1 compare the 2 data sets with simulations.

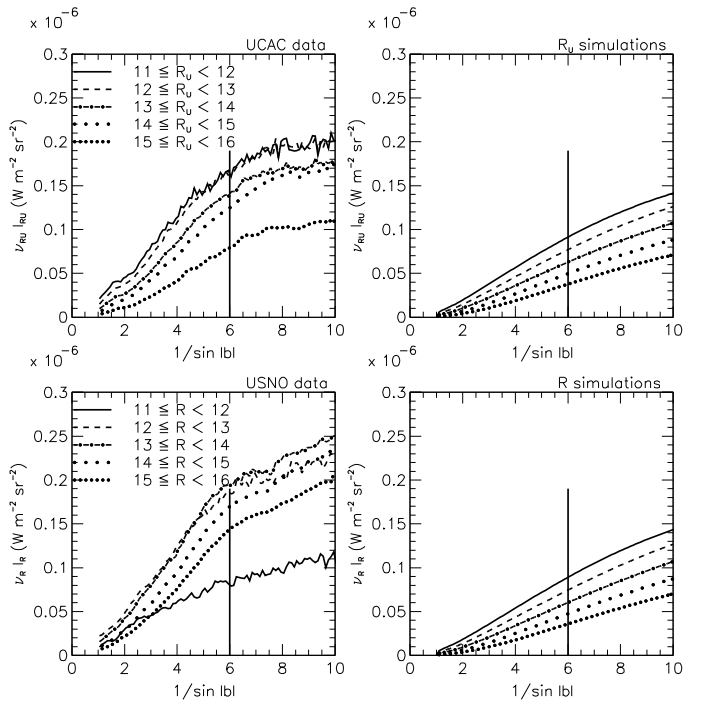


Fig. F.2. Integrated R flux as a function of $1/\sin(|b|)$ for the UCAC (top) and USNO-A2 (bottom) stars lying in the UCAC-1 area defined in Fig. F.1. These fluxes correspond to the contribution of this area to the total flux received at the Sun. No correction has been applied. The results of the fits for $1/\sin(|b|) < 6$ are provided in Table F.1.

Table F.1. R_U (UCAC-1) and R (USNO-A2) fluxes, given in $10^{-9}\text{W m}^{-2} \text{sr}^{-1}$. We give the values (2) and (3) fitted to R_U (UCAC-1) and R (USNO-A2) fluxes for $1/\sin|b| < 6$ (see Fig. E.1) over the area defined in Fig. F.1, for each magnitude bin (1). Last, we provide the ratio (4) between the UCAC-1 and USNO-A2 slopes. No correction is applied.

Magnitude range (1)	$ b = 90^\circ$ (2)	Slope (3)	$ b = 90^\circ$ (4)	Slope (5)
UCAC-1 data				R_U Simulation
$8 \leq R_U < 9$	22.49	8.07	7.32	31.20
$9 \leq R_U < 10$	31.98	16.38	5.74	26.86
$10 \leq R_U < 11$	26.88	25.62	4.22	22.22
$11 \leq R_U < 12$	17.56	31.55	2.87	17.50
$12 \leq R_U < 13$	7.72	32.98	1.80	12.99
$13 \leq R_U < 14$	0.03	28.88	1.03	9.06
$14 \leq R_U < 15$	-3.95	25.61	0.55	5.90
$15 \leq R_U < 16$	-4.87	16.36	0.29	3.59
USNO-A2 data				R_C Simulation
$11 \leq R < 12$	13.51	15.16	2.87	17.50
$12 \leq R < 13$	14.94	35.80	1.80	12.99
$13 \leq R < 14$	4.00	39.58	1.03	9.06
$14 \leq R < 15$	-4.45	34.63	0.55	5.90
$15 \leq R < 16$	-7.39	29.38	0.29	3.59

Appendix G: Calibration of the USNO-A2 data

Given the dispersion of USNO-A2 magnitudes, accounting for colour effects would introduce an additional source of noise for single wavelength flux measurements. As we are interested in integrating the total flux at given wavelengths, we deliberately neglect colour effects and perform the calibration between single filters. The red measurements correspond to the plate emulsions 103a-E (North) and IIIa-F (south). The equivalent wavelengths are respectively 6450 Å and 6400 Å which are very close to the R_C filter. The blue measurements (103a-O (POSS-I O) for the North, and IIIa-J (POSS-I E) for the south) differ more significantly with equivalent wavelengths of 4050 Å and 4680 Å. We estimate that a 10% uncertainty is introduced when aligning these measurements to the B_J data, which remains negligible for our purposes.

We cross-identify the 526 280 881 USNO-A2 stars (Monet et al. 1998) with those of the GSPC2.1 catalogue (Buccarelli et al. 2001) composed of 305 017 stars with CCD (B)VR photometry within a $5'' \times 5''$ window. In the USNO-A2 catalog, the sky is partitioned into 24 zones of South Polar Distance (SPD), each of width 7.5° . We thereby find 257 352 stars spread over 21 zones. For each zone, we plot the residuals in RA and DEC, and keep the 186 568 stars within 1σ of the mean of each zone. We then compute the relationships between different magnitude systems as shown in Figure G.1. The corresponding coefficients are provided in Table G.1. B_{USNO} and R_{USNO} magnitudes are thus converted into B_J ($\lambda_o^B = 4400$ Å) and R_C ($\lambda_o^R = 6400$ Å) magnitudes, which are in turn converted into fluxes with $F_{B,R} = C_{B,R} 10^{-0.4 \times B,R}$ ($C_B = 4.26 \times 10^{-23} \text{ W m}^{-2} \text{ Hz}^{-1}$, $C_R = 3.08 \times 10^{-23} \text{ W m}^{-2} \text{ Hz}^{-1}$).

Note that we do not detect any significant bias between northern and southern hemispheres. Systematic effects are observed for R_{USNO} data for $R_{\text{USNO}} > 17.5$ and $\delta < -14^\circ$. They will tend to overestimate the contribution of faint stars and are most probably an effect of crowding.

Table G.1. Coefficients used for the calibration of the USNO magnitudes. In blue (B), $B_J = \alpha + \beta(B_{\text{USNO}} - 15) + \gamma(B_{\text{USNO}} - 15)^2$. In red (R), $R_C = \alpha + \beta(R_{\text{USNO}} - 15) + \gamma(R_{\text{USNO}} - 15)^2$. The columns are defined as follows: (1) the zone number, (2) the declination band covered, (3) the filter used, (4) α , (5) β , (6) γ , (7) the RMS error of the polynomial fit, (8) the number of stars effectively used in the fit. We thus used 104 354 stars in blue and 154 491 stars in red.

Zone	DEC	Filters	α	β	γ	Residuals	N_{stars}
075	-82.5° to -75.0°	B	15.24	1.14	0.0	0.38	1111
		R	15.06	1.02	6.99×10^{-2}	0.34	724
150	-75.0° to -67.5°	B	15.59	0.95	2.32×10^{-2}	0.45	2048
		R	15.05	1.01	7.68×10^{-1}	0.42	1320
225	-67.5° to -60.0°	B	15.80	1.00	-1.67×10^{-1}	0.67	2006
		R	14.92	0.97	6.45×10^{-2}	0.41	1653
300	-60.0° to -52.5°	B	15.22	1.16	0.0	0.42	2509
		R	15.04	0.95	8.09×10^{-2}	0.36	2204
375	-52.5° to -45.0°	B	15.48	1.09	0.0	0.40	3488
		R	15.03	0.99	7.31×10^{-2}	0.38	1949
450	-45.0° to -37.5°	B	15.27	1.15	0.0	0.36	2206
		R	15.05	0.98	5.13×10^{-2}	0.33	1220
525	-37.5° to -30.0°	B	15.47	1.03	9.07×10^{-3}	0.50	7590
		R	14.90	0.88	8.26×10^{-3}	0.47	5061
600	-30.0° to -22.5°	B	15.63	1.00	9.59×10^{-3}	0.48	8879
		R	15.01	0.94	4.88×10^{-2}	0.40	5771
675	-22.5° to -15.0°	B	15.58	1.00	1.44×10^{-2}	0.42	6065
		R	14.99	0.95	3.96×10^{-2}	0.42	4578
750	-15.0° to -7.5°	B	15.60	1.05	0.0	0.38	4196
		R	15.16	0.92	1.21×10^{-2}	0.41	6624
825	-7.5° to 0.0°	B	15.39	1.06	0.0	0.33	2470
		R	15.07	0.97	0.0	0.34	3949
900	0.0° to 7.5°	B	15.39	1.07	0.0	0.30	2171
		R	15.09	0.99	0.0	0.33	5047
975	7.5° to 15.0°	B	15.68	1.00	0.0	0.34	8428
		R	15.13	0.97	0.0	0.33	14084
1050	15.0° to 22.5°	B	15.47	0.94	2.69×10^{-2}	0.38	5945
		R	15.11	0.95	1.68×10^{-2}	0.39	11035
1125	22.5° to 30.0°	B	15.28	1.05	9.92×10^{-3}	0.33	7549
		R	15.11	0.96	1.47×10^{-2}	0.33	12974
1200	30.0° to 37.5°	B	15.21	1.13	-6.01×10^{-3}	0.28	12011
		R	15.11	0.96	8.08×10^{-3}	0.33	17769
1275	37.5° to 45.0°	B	15.40	0.99	1.68×10^{-2}	0.33	12665
		R	15.02	0.94	1.37×10^{-2}	0.39	21022
1350	45.0° to 52.5°	B	15.34	1.08	0.0	0.32	9248
		R	15.07	0.97	4.56×10^{-3}	0.39	17967
1425	52.5° to 60.0°	B	15.65	1.08	-3.69×10^{-2}	0.76	3720
		R	15.12	0.93	0.0	0.55	8983
1500	60.0° to 67.5°	B	15.23	1.15	-1.08×10^{-2}	0.31	6468
		R	15.10	0.95	0.0	0.43	9996
1575	67.5° to 75.0°	B	15.65	1.16	-2.03×10^{-2}	0.25	412
		R	14.61	1.00	2.90×10^{-2}	0.56	1031

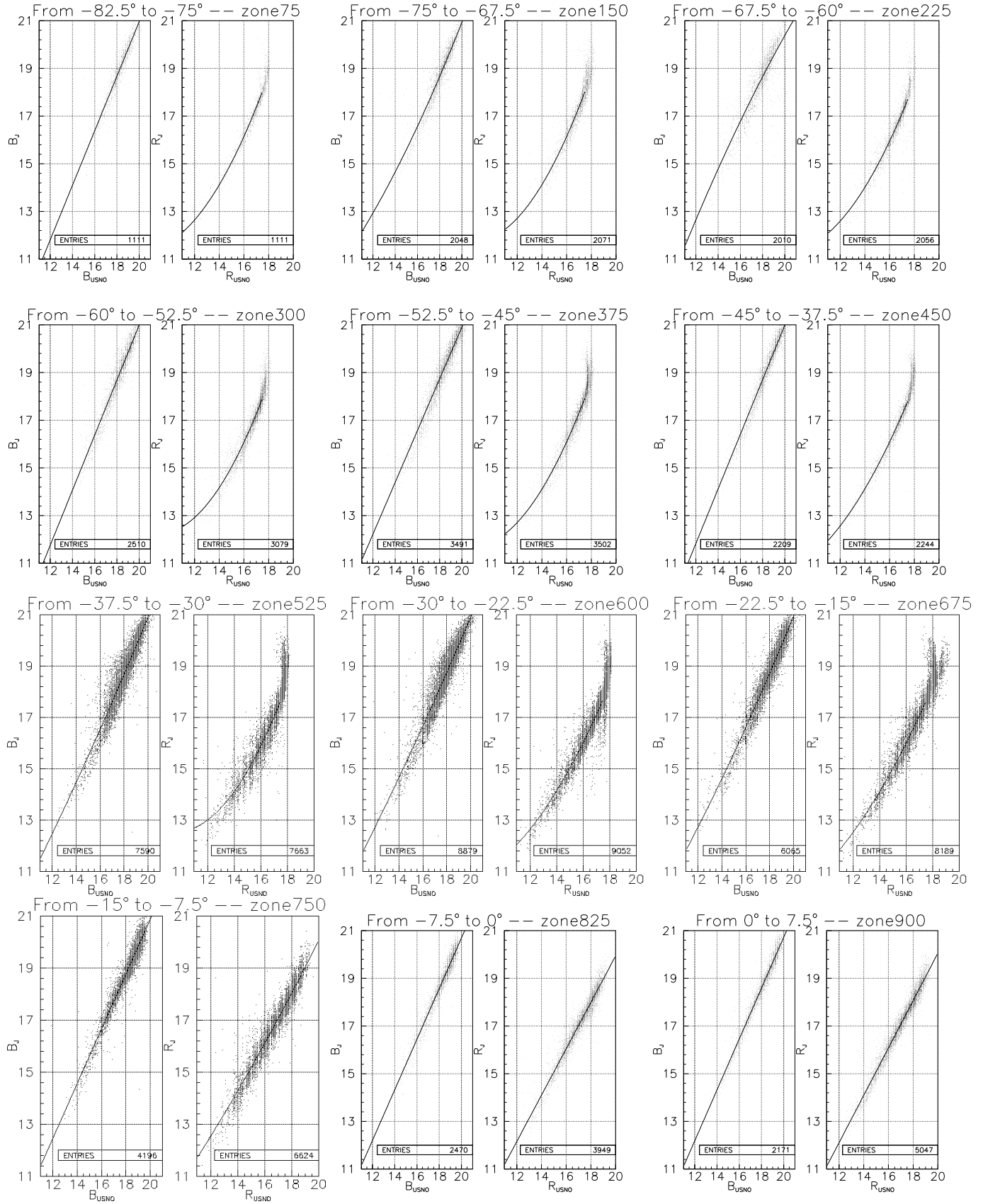
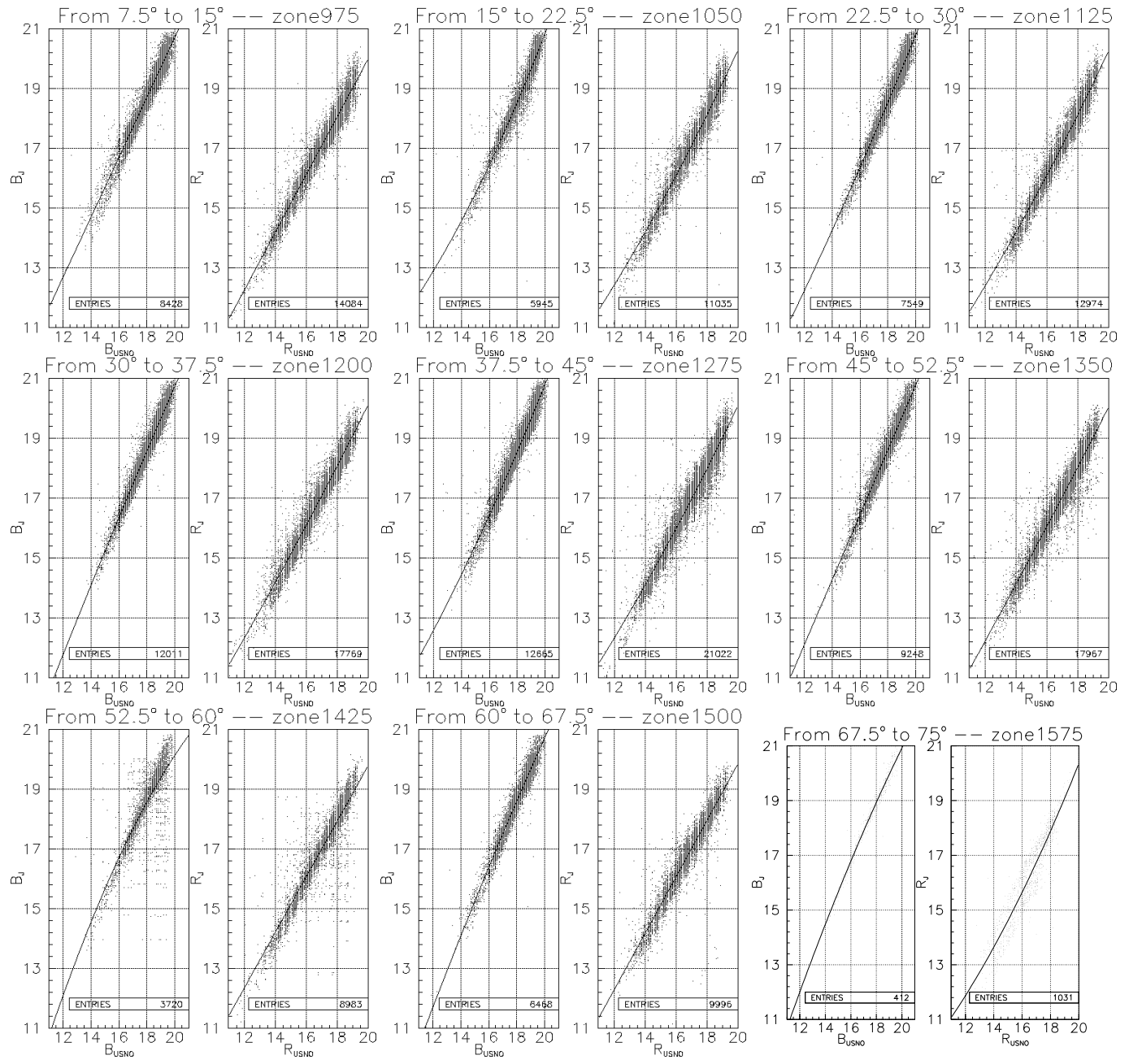


Fig. G.1. Each panel presents the B_J versus B_{USNO} and R_C versus R_{USNO} relations for each South Polar Distance (SPD) interval corresponding to a zone. The polynomial adjustments are superimposed for each relation, and the corresponding coefficients are provided in Table E.1.

**Fig. G.1.** Continued